

TOF-SIMS analysis of crater residues from Wild 2 cometary particles on Stardust aluminum foil

Jan LEITNER^{1†*}, Thomas STEPHAN^{1††}, Anton T. KEARSLEY², Friedrich HÖRZ³,
George J. FLYNN⁴, and Scott A. SANDFORD⁵

¹Institut für Planetologie, Westfälische Wilhelms-Universität Münster, Wilhelm-Klemm-Str. 10, 48149 Münster, Germany

²Impact and Astromaterials Research Centre, Department of Mineralogy, The Natural History Museum, London SW7 5BD, UK

³NASA Johnson Space Center, Houston, Texas 77058, USA

⁴Department of Physics, SUNY Plattsburgh, Plattsburgh, New York 12901, USA

⁵Astrophysics Branch, NASA Ames Research Center, Moffett Field, California 94035, USA

[†]Present address: Max Planck Institute for Chemistry, Particle Chemistry Department, P.O. Box 3060, 55020 Mainz, Germany

^{††}Present address: Department of the Geophysical Sciences, University of Chicago, 5734 South Ellis Avenue, Chicago, Illinois 60637, USA

*Corresponding author. E-mail: leitner@mpch-mainz.mpg.de

(Submitted 15 December 2006; revision accepted 24 May 2007)

Abstract—Impact residues of cometary particles on aluminum foils from the Stardust mission were investigated with TOF-SIMS for their elemental and organic composition. The residual matter from comet 81P/Wild 2 shows a wide compositional range, from nearly monomineralic grains to polymict aggregates. Despite the comparably small analyzed sample volume, the average element composition of the investigated residues is similar to bulk CI chondritic values. Analysis of organic components in impact residues is complicated, due to fragmentation and alteration of the compounds during the impact process and by the presence of contaminants on the aluminum foils. Nevertheless, polycyclic aromatic hydrocarbons (PAHs) that are unambiguously associated with the impact residues were observed, and thus are most likely of cometary origin.

INTRODUCTION

In January 2006, the Stardust mission returned cometary matter to Earth that was collected during the spacecraft's passage through the coma of comet 81P/Wild 2 in January 2004 (Brownlee et al. 2003; Tsou et al. 2003). These samples offer the first opportunity to analyze cometary matter collected under controlled conditions from a specific comet. During the cruise phase, before the cometary encounter, Stardust also collected contemporary interstellar dust on the rear side of the collector tray.

Stardust used two different types of capture media for both cometary and interstellar dust. Low-density, SiO₂-based aerogel was used as the primary medium to gently decelerate the impinging particles more or less intact (Tsou et al. 2003). In contrast, on the second capture medium, aluminum foil (Al 1100; >99% pure), particles came to an abrupt stop and produced hypervelocity craters. These foils were mainly used to facilitate the removal of the aerogel tiles from the modular collector trays following return to Earth (Tsou et al. 2003). However, Al foil exposed to the comet also provided a valuable capture medium (Hörz et al. 2006), since impactor residues were found, typically as discontinuous layers of shock-produced melts, inside crater cavities or on crater rims.

In the present study, residual cometary matter in craters on the Stardust Al foils was analyzed by time-of-flight secondary ion mass spectrometry (TOF-SIMS) in order to determine the elemental and organic composition of the dust and thereby properties of the cometary nucleus itself. Earlier investigations (Stephan et al. 2005; Hoppe et al. 2006; Leitner et al. 2006a, 2006b) on experimental craters have shown that from the elemental composition of the residual matter in craters, the projectile material can be identified and its composition can be revealed, despite the significant, shock-induced alterations at the Stardust encounter speed of 6.12 km s⁻¹.

SAMPLES AND EXPERIMENTAL METHODS

Nine foils from the cometary side of the sample tray assembly (STA) of the Stardust spacecraft were selected for TOF-SIMS analysis: C2009N,1, C2026N,1, C2029W,1, C2070W,1, C2086N,1, C2086W,1, C2091N,1, C2101W,1, and C2102W,1. Only foils C2009N,1, C2029W,1, C2086N,1, C2086W,1, C2091N,1, and C2102N,1 contained craters with diameters >10 μm, as illustrated in Fig. 1.

Since these foils were not perfectly flat after cutting

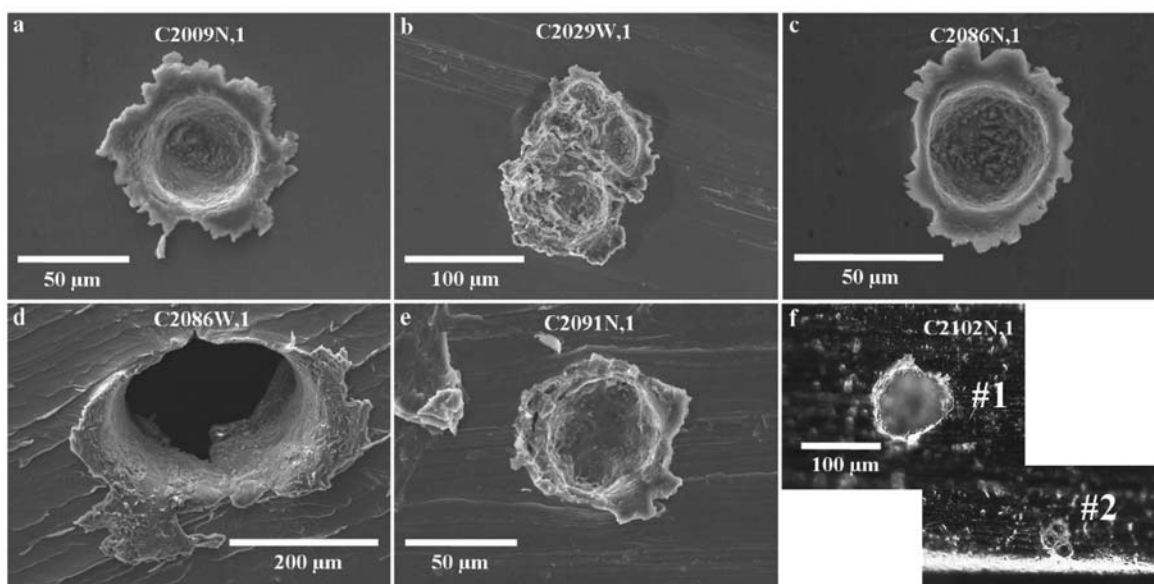


Fig. 1. Secondary electron (a–e) and optical microscope (f) images of Stardust craters on Al foil investigated in this study. For C2102N,1, no secondary electron images were available.

and removal from the STA by NASA's curatorial staff, they had to be flattened prior to detailed analyses. This was achieved by slightly stretching the foils by $\sim 2.5\%$, which was carried out by F. J. Stadermann at Washington University, St. Louis, Missouri. After straightening, the samples were analyzed using a TOF-SIMS IV instrument from ION-TOF equipped with a gallium liquid metal ion source for SIMS analysis and an argon ion source for sputter cleaning. TOF-SIMS usually requires flat surfaces. Obviously, Al foil craters, even after flattening of the foils, are not perfectly flat. The remaining surface topography slightly degraded the mass resolution $(m/\Delta m)_{\text{FWHM}}$ from ~ 5500 to ~ 4000 at mass 29 u for craters in the 100 μm size range. Further topographic effects are well understood and have been described in the literature (Rost et al. 1999). However, one has to keep in mind that the primary ions reach the sample at a 45° angle, which leads to certain distortions in the secondary ion images from the craters, which are explained in Figs. 2a–c. Secondary ions sputtered from positions marked by the numbered points in Fig. 2b seem therefore to stem from the positions displayed in Fig. 2c. So, points 5–10 seem to be from the bottom of the crater, while most of them are actually from the crater rim. Also, secondary ions from point 2 are projected onto the rim, while ions originating from below the crater lip are shielded and thus not detected, producing a shadow on this side of the crater although the primary beam is scanning from this direction. Furthermore, not all sample regions in the crater or on the crater rim can be accessed by the ion beam in any single measurement. Therefore, selected craters were analyzed twice, in different orientations, to provide access to a larger portion of the residues in these craters.

To remove an omnipresent, thin contamination layer, the sample surfaces had to be cleaned by Ar^+ ion bombardment prior to measurement. To ensure proper cleaning of the non-flat craters, the sample was rotated four times by 90° during this procedure. On the other hand, complex molecular ions like, e.g., polycyclic aromatic hydrocarbons (PAHs) are destroyed during this process. Therefore, TOF-SIMS measurements were carried out before and after sputter cleaning.

During the analyses, individual sample areas were rastered (128^2 , 256^2 , or 512^2 pixels) with a $\sim 0.3 \mu\text{m}$ $^{69}\text{Ga}^+$ primary ion beam with a repetition rate of 10 kHz and a pulse width of ~ 1.5 ns.

Based on the lateral distributions of secondary ions of the major elements Mg, Si, Ca, and Fe, and in some cases Cr, Mn, and Ni, as judged from qualitative elemental maps, regions of interest were selected for the generation of quantitative mass spectra and determination of element ratios using relative SIMS sensitivity factors derived from glass standards. The uncertainty for such an approach is expected to be of the order of a factor of <1.5 . Further details are given in the literature (Stephan 2001; Hoppe et al. 2006). All abundances reported here are atomic element ratios relative to Si and, in some cases, normalized to CI chondritic composition.

Because the impinging cometary dust particles and their melts have incorporated variable amounts of foil material, the elemental composition of the crater residues obtained from the analyses does not resemble exactly the original composition of the impactors. Thus, a data correction using elemental ratios from the surrounding aluminum blank was applied as described by Hoppe et al. (2006).

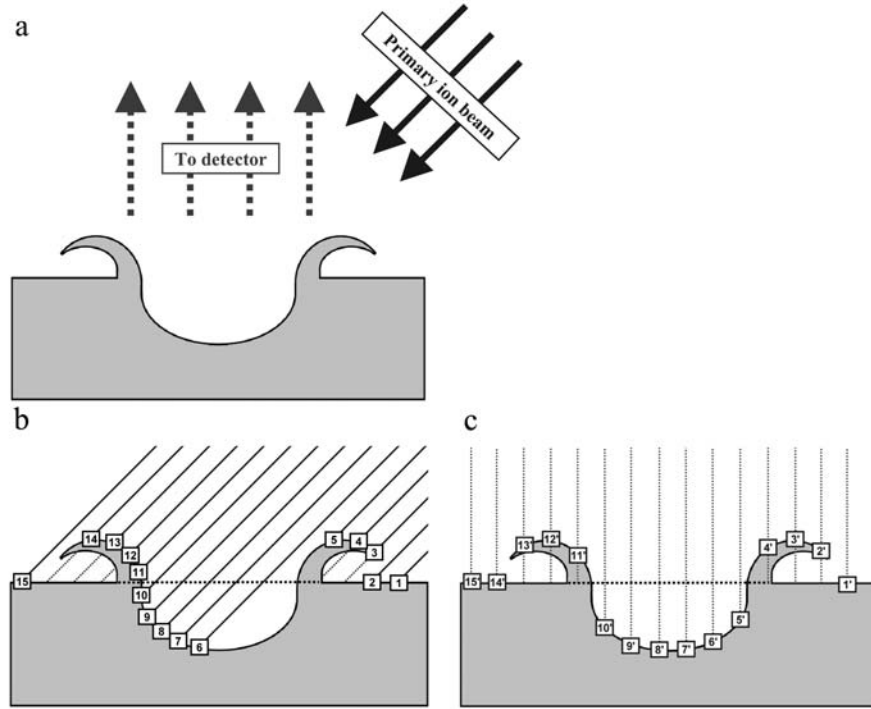


Fig. 2. a) Due to the instrumental geometry, the rastered primary ion beam reaches the sample surface under a 45° angle, while the secondary ion extraction is normal to the surface plane. This leads to apparent distortions in the secondary ion images from non-flat samples. b) The black lines show equidistant primary beams that are rastered over the sample surface. Numbered points indicate from where on the sample secondary ions are released and subsequently analyzed in the mass spectrometer. c) An observer assumes that the primary ion beam scans the crater in equidistant steps from his point of view, as indicated by the dotted lines. So the secondary ions seem to originate from the numbered points shown in this image.

Blank Correction

From its chemical properties, Stardust Al foil is nearly pure Al. However, it is contaminated with traces of other elements, and correction for a foil blank had to be performed, because the cometary matter analyzed in this study is intimately mixed with foil material. Therefore, the composition of the foil close to each investigated crater was also determined.

After selecting a region of interest containing the residual projectile matter, the fraction of every individual element that belongs to the cometary residue has to be determined. Any given element E consists of a fraction E_r that stems from this residue and another one that is inherent in the foil blank, E_b :

$$E = E_r + E_b. \quad (1)$$

Since one is interested in the silicon-normalized abundance, one searches for $(E/Si)_r$. This term can be written as:

$$\frac{E_r}{Si_r} = \frac{E}{Si_r} - \frac{E_b}{Si_r} \quad (2)$$

and then transformed into:

$$\begin{aligned} \frac{E_r}{Si_r} &= \frac{E/Si}{Si_r/Si} - \frac{E_b/Si_b}{Si_b/Si_r} \\ &= \frac{E/Si}{Si_r/Si} - \frac{E_b}{Si_b} \left(\frac{Si}{Si_r} - \frac{Si_r}{Si} \right) \end{aligned} \quad (3)$$

and finally:

$$\left(\frac{E}{Si} \right)_r = \frac{E/Si}{Si_r/Si} - \left(\frac{E}{Si} \right)_b \left(\frac{1}{Si_r/Si} - 1 \right) \quad (4)$$

The fraction of silicon that belongs to the cometary particle Si_r/Si has to be determined, since silicon is used as reference element throughout this study. From Equation 4, one can derive for $E = Al$

$$\frac{Si_r}{Si} = \frac{\frac{Al}{Si} - \left(\frac{Al}{Si} \right)_b}{\left(\frac{Al}{Si} \right)_r - \left(\frac{Al}{Si} \right)_b} \quad (5)$$

With Equations 4 and 5, $(E/Si)_r$ can be derived from measured quantities if $(Al/Si)_r$ is known. Since the initial composition of a captured cometary particle is unknown, one

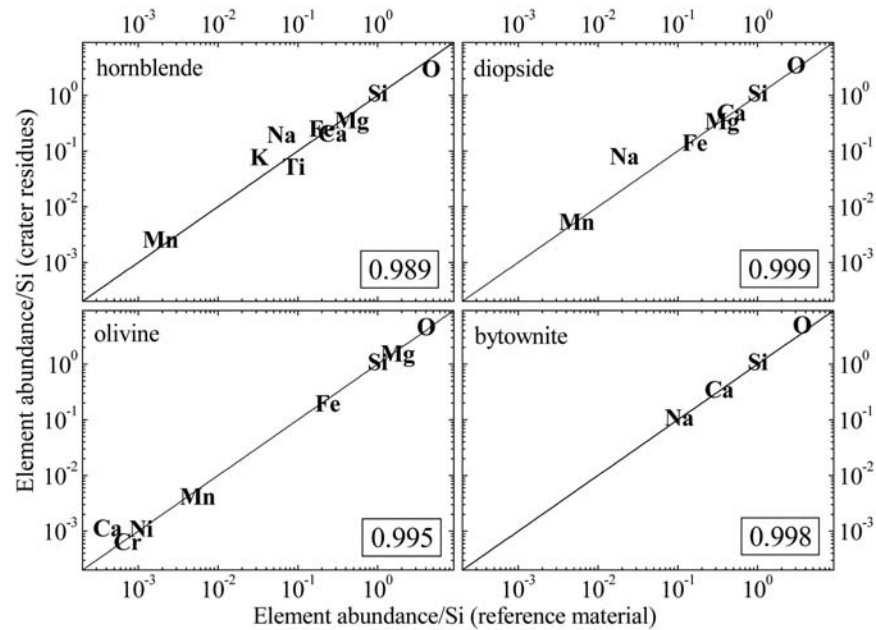


Fig. 3. Element abundances of crater residues of four analyzed mineral standards (hornblende, diopside, olivine, and bytownite) in comparison with reference data of these materials. Additionally, correlation coefficients for each residue and the according reference data are displayed.

may assume that the sample has a CI-like Al/Si ratio of ~ 0.0849 (Anders and Grevesse 1989).

Certainly, the use of CI chondritic Al/Si ratios is only a first-order approximation. However, this assumption does not imply that Wild 2 material is expected to be similar in mineralogy to CI chondrites, but CI chondritic abundances are used in this study as an approximation for solar system abundances.

For all investigated sample areas, >96% of the aluminum stems from the foil blank. Therefore, an uncertainty in the indigenous Al/Si ratio has only a minor effect on the determined element ratios, smaller than the statistical errors, and the CI approximation is certainly valuable. Even with the assumption that there was no indigenous Al at all in the cometary particles, the corrected data would deviate less than 7% from the CI-corrected values. So, it makes only little practical difference what cometary Al is assumed, since the Al is so strongly dominated by the blank signal that these variations contribute only small modifications to the blank correction.

The order of magnitude of the blank corrections shows some variation, depending on the abundance of the element in the residue as well as on the level of contamination from the surrounding foil blank. The tables in the appendix give detailed information on the uncorrected data, foil blank data, and blank corrected data applied in this study.

Although the bulk foil composition can be determined with good confidence and displays no pronounced variations (Kearsley et al. 2006, 2007), individual foils and even different areas of the same foil show nevertheless large variations in their local surface compositions. This heterogeneity can have a great influence on the analytical results obtained by

TOF-SIMS, since this technique is extremely surface sensitive. Typically, only the upper 3–5 monolayers of a sample are analyzed, so that the investigated sample volume is by orders of magnitude smaller than for comparable SEM-EDX analyses. For the blank correction, only the element composition derived from TOF-SIMS analyses of the foil blank in the crater's vicinity was used by applying appropriate regions of interests. All data were discarded wherever the blank signal was found to be higher than 50% of the entire signal or where the lateral distribution of the contamination was obviously heterogeneous, and therefore a clear attribution of the measured signal to cometary material could not be made.

Analysis of Standards

Prior to analyzing the Wild 2 samples, several standards of well-known compositions were shot at 4.2–6.1 km s⁻¹ into aluminum foil and investigated by TOF-SIMS (Stephan et al. 2005; Hoppe et al. 2006; Leitner et al. 2006a, 2006b) to evaluate the reproducibility of the chemical composition of the projectile materials by TOF-SIMS analysis. These standards included powders from the CV chondrite Allende, as reported earlier (Stephan et al. 2005; Hoppe et al. 2006), and were extended in this study, using light gas guns at NASA Johnson Space Center and University of Kent, to hornblende (USNM 143965), and four well-characterized mineral powders from the hypervelocity projectile collection of the Natural History Museum in London: diopside (BM.2005,M310 from Yates Mine, Quebec, Canada), olivine (BM.1950,337 from the Admire pallasite meteorite), bytownite (BM.2005,M312, from Majorqap qava in Greenland), and

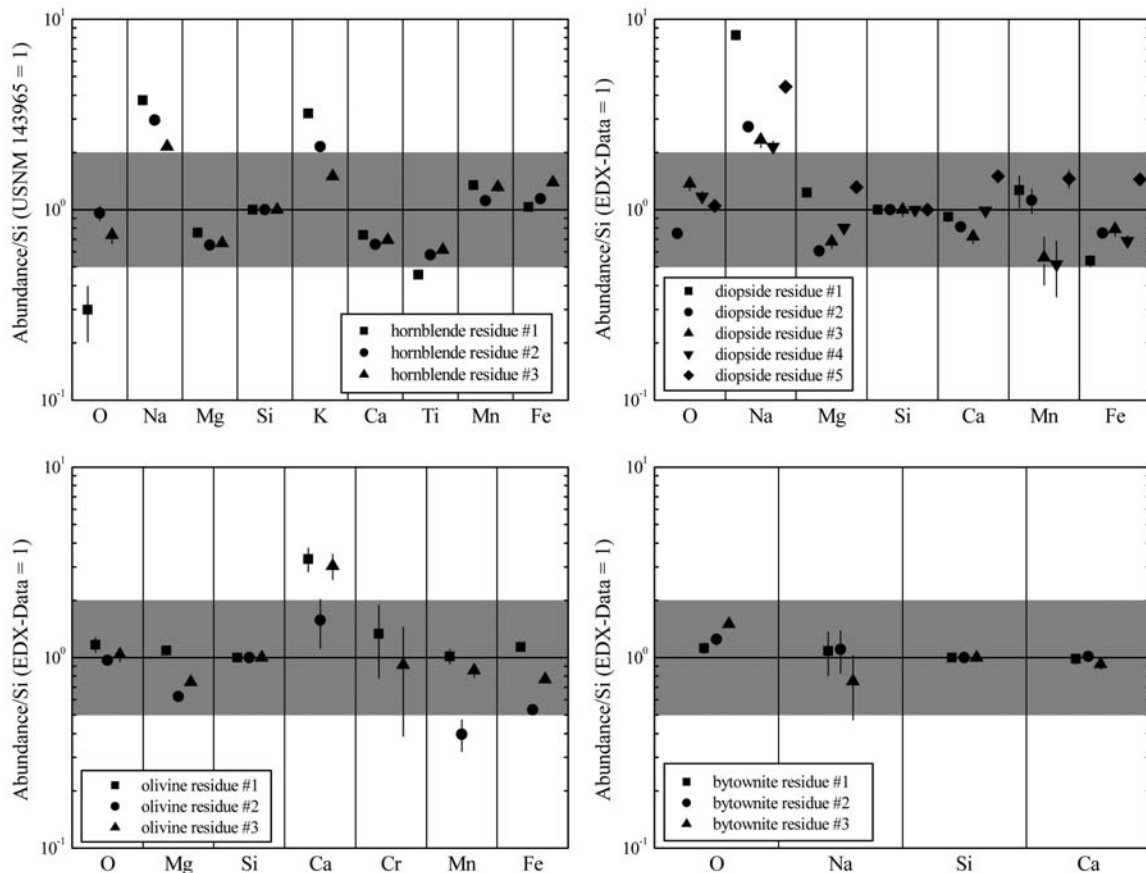


Fig. 4. Element abundances relative to Si and normalized to literature values or SEM-EDX analytical results for mineral standards. The gray bars mark the range between 0.5 and 2 times the reference values.

pyrrhotite (BM.2005,M317 from Drag in Norway). The four foils impacted by anhydrous mineral powders are segments of the same samples described in the crater morphology and residue studies of Kearsley et al. (2007).

The blank correction for the mineral standards was calculated as described above, with Al/Si ratios obtained from reference data like SEM-EDX-analyses used instead of a Cl-like Al/Si ratio.

RESULTS

Mineral Standards

Quantitative results obtained from mineral standards are summarized in Figs. 3 and 4. All single-mineral standards could be identified unambiguously from the TOF-SIMS analysis of their crater residues. In comparison to their element ratios from literature data or SEM-EDX data (Kearsley et al. 2007), correlation coefficients >0.989 were found (Fig. 3).

These reference measurements suggest that there are no major modifications of the impactor composition during the impact process at velocities up to 6.1 km s^{-1} , at least for the

major elements. The largest deviations from the nominal values occur only for some minor constituents of the minerals with abundances of less than 1 wt%. Na and K in the investigated hornblende standard are 0.96 wt% and 0.85 wt%, respectively, the diopside contains $0.43 \pm 0.06 \text{ wt% Na}$, and the olivine contains $0.011 \pm 0.005 \text{ wt% Ca}$. These elements may be affected by mobilization effects. In a previous study, modest to significant loss of Na and K, in combination with an increase in refractory elements, especially Ca, in the impact melts was observed (Hörz et al. 1983; Kearsley et al. 2007).

This fractionation effect was reported for the main fraction of the residue inside the impact craters. The increased alkali abundances in the residue on the crater lips (Fig. 4), the areas accessible for TOF-SIMS analysis, possibly are the result of recondensation of mobilized volatiles on the crater rim. The SIMS study of Amari et al. (1991) reported evidence of elemental fractionation around hypervelocity impact features on the Long Duration Exposure Facility spacecraft. However, these structures are likely to have formed at much higher impact velocity ($25\text{--}70 \text{ km s}^{-1}$) than craters on Stardust foil, and may therefore have undergone a much greater degree of processing. Nevertheless, for the bytownite mineral standard with $\sim 2 \text{ wt% Na}$, no deviation between TOF-SIMS

Table 1. Atomic element ratios relative to Si and solar system abundances and corrected for Al foil blanks for crater residues #2.1, #2.2, #2.3, as well as the bulk residue composition of C2102N,1 #2. Statistical errors are given as last significant digit in parentheses.

	C2102N,1 #2.1	C2102N,1 #2.2	C2102N,1 #2.3	C2102N,1 #2
Li		2(1)	2.4(6)	1.9(6)
Na	49.7(1)	15.0(1)	10.48(3)	18.72(3)
Mg	2.45(1)	1.29(1)	1.060(4)	1.450(4)
Si	1.00(4)	1.00(3)	1.00(1)	1.00(2)
K	16.2(2)	10.0(2)	5.8(1)	9.0(1)
Ca	5.29(6)	2.09(3)	1.81(1)	2.69(2)
Sc	3(3)	2(2)	3(1)	4(1)
Ti			0.6(2)	
Cr	0.74(8)	0.45(5)	0.64(3)	0.70(3)
Mn	1.01(1)	0.75(8)	0.61(4)	0.79(4)
Fe	2.1(1)	0.59(5)	0.34(2)	0.76(3)
Co	0.5(3)	1.7(4)	0.4(1)	0.8(1)
Ni	0.5(1)	2.3(2)	0.8(1)	1.1(1)

Table 2. Atomic element ratios are shown relative to Si and corrected for Al foil blanks for the analyzed crater residues. Statistical errors are given as last significant digit in parentheses.

	C2009N,1	C2029W,1 (0°)	C2029W,1 (180°)	C2086N,1	C2086W,1 (0°)	C2086W,1 (180°)	C2091N,1	C2102N,1 #1	C2102N,1 #2
Li	0.00017(2)	0.0037(5)	0.0008(2)	0.00003(2)		0.00011(5)	0.00014(3)	0.00021(1)	0.00011(3)
Na	0.0854(4)	10.04(2)	1.400(5)	0.0353(4)	0.456(1)	1.276(3)	0.463(1)	0.5469(5)	1.075(2)
Mg	0.829(2)	24.49(6)	4.31(2)	1.202(4)	0.393(3)	0.527(4)	1.069(3)	1.377(1)	1.552(4)
Si	1.00(1)	1.00(7)	1.00(4)	1.00(2)	1.00(2)	1.00(1)	1.00(1)	1.00(1)	1.00(2)
K	0.0104(1)	0.601(4)	0.048(1)	0.0035(1)		0.0177(4)		0.0512(1)	0.0339(3)
Ca			1.71(1)	0.215(3)		0.0453(8)	0.0448(8)	0.0957(3)	0.164(1)
Sc		0.0008(4)	0.0004(2)	0.00003(2)	0.00004(3)		0.00009(3)		0.00012(4)
Ti	0.0011(1)			0.0011(2)		0.0026(4)			
Cr	0.0075(2)			0.0072(3)		0.0012(3)	0.0061(4)	0.0062(1)	0.0094(4)
Mn	0.0047(2)	0.008(2)	0.0052(8)	0.0014(2)	0.0152(7)	0.0058(6)		0.0043(1)	0.0075(4)
Fe	0.24(1)	0.90(3)	0.24(1)	0.032(1)	0.389(4)	0.516(7)	0.26(2)	0.176(2)	0.68(3)
Co	0.0006(1)	0.009(2)	0.015(2)				0.0003(1)		0.0018(3)
Ni	0.113(3)	0.19(2)	0.051(6)	0.0008(5)	0.013(3)	0.008(3)	0.010(2)	0.014(1)	0.055(5)

data of impact residues and SEM-EDX data was observed. Therefore, it seems to be plausible that for impacts onto foil at 6 km s⁻¹, extensive mobilization and recondensation processes affect only volatiles that occur in associated traces, and not those elements that are bound tightly within the mineral structure.

Furthermore, Na, K, and Ca may be influenced by contamination present on the foils. Figure 5 shows examples from three craters for such heterogeneously distributed elements in the Al foil blank. For all craters, significant abundances of the displayed ion species are present in the vicinity of each crater.

Foils without Large Craters—C2026N,1, C2070W,1, and C2101W,1

No craters with diameters >10 μm were found on these foils. Instead, a variety of features was observed: depressions and scratches in the Al foils, deposits and grains on the foil surfaces, as well as impurities inherent to the Al foils.

Secondary ion images are displayed in Figs. 6–8. Analyses were carried out to determine the nature of these features, so that a discrimination between surface contaminants like aerogel debris, common Al foil impurities that may influence the compositions of impact residues from cometary particles, and potential deposits from primary cometary particle impacts on the foils is possible.

Figures 6a and 6b show examples of surface deposits and foil impurities observed on foil C2026N,1. In Fig. 6a, a Si- and Ca-rich area is visible. The low intensity of Al⁺ in this region indicates that the Si- and Ca-bearing structure is a particle located on the foil surface covering the Al foil. Furthermore, a second hotspot containing Mg and Si is also visible in Fig. 6a. The SI images in Fig. 6b show another hotspot on the same foil. It contains Na, Mg, Si, K, Ca, Fe, and Tl. The identification of Tl was unambiguous, since both isotopes with masses of 203 u and 205 u were present, and the measured ratio of ²⁰⁵Tl/²⁰³Tl = 2.3 ± 0.1 is within error limits identical to the terrestrial value of 2.39. As in Fig. 6a, the spot of low

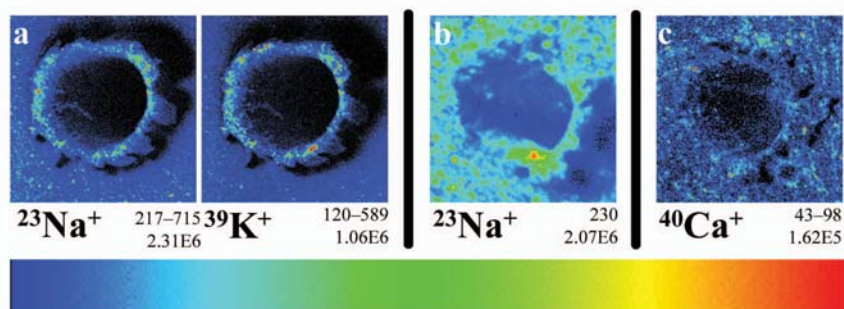


Fig. 5. Secondary ion images of crater residues of several mineral standards. The ion species is mentioned below each image. Also below each image are the maximum intensity per pixel or an intensity range, to which the ion image is normalized, and the integrated intensity of the whole image. The color bar represents a linear scale from black (zero intensity) to red (maximum intensity). All subsequent secondary ion images are displayed in this way. a) Crater from a hornblende projectile, field of view is $350 \times 350 \mu\text{m}^2$. b) Crater produced by a diopside projectile, field of view is $43.5 \times 43.5 \mu\text{m}^2$. c) Olivine crater residue, field of view is $103 \times 103 \mu\text{m}^2$.

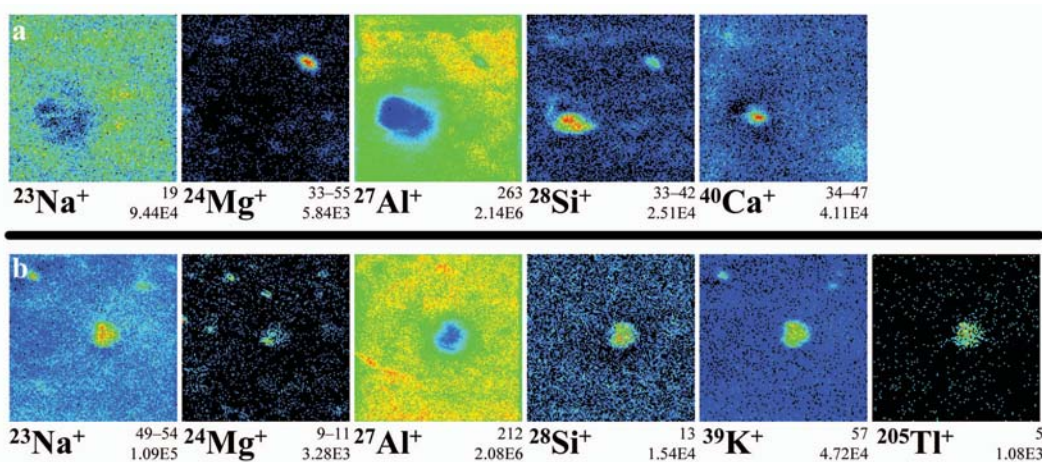


Fig. 6. Secondary ion images of different contamination features, not correlated to impact craters, found on foil C2026N,1. a) Field of view is $13.4 \times 13.4 \mu\text{m}^2$; b) field of view is $15.2 \times 15.2 \mu\text{m}^2$.

intensity in the Al^+ image indicates that this spot is actually a deposit covering the foil surface.

In Figs. 7a–f, several features located on foil C2070W,1 are displayed. Figures 7a, 7b, and 7c show examples for deposits that were identified by their compositions as aerogel debris, since the main constituents besides Si are hydrocarbons. In Fig. 7d, scattered hotspots of several elements can be seen. Correlations exist for Mg and Ti as well as for Ni and Cu, respectively.

Figures 7e and 7f show secondary ion images of two regions on foil C2070W,1 with correlated Mg and Si hotspots. Although Na, K, Ca, and Ti have similar lateral distributions in the area shown in Fig. 7e, there is no correlation of these elements with Mg and Si. For Fig. 7f instead, especially Ti, but also Na, K, and Ca are distributed quite similar to Mg and Si.

In Fig. 8, some examples of the Si-rich contaminations on foil C2101W,1 can be seen. Figures 8a, 8c, and 8d show typical element distributions for aerogel debris, i.e., the areas of low Al abundance correlate with high Si intensities. Figure 8b, on the

other hand, shows a different distribution: The area in the center of the Al^+ secondary ion image with nearly no signal intensity seems to be a dent in the foil with a Si containing scratch at its upper left corner, since no other ion species was detected in this area, except for three Ti spots.

One likely source of contamination on the aluminum foils is small fragments of the nearby aerogel. Since the Mg/Si ratio of Stardust aerogel is very low (Tsou et al. 2003; Stephan et al. 2008), we separate the Si-rich deposits and grains into two groups, one with relatively high Mg/Si, and a second with very low Mg/Si, potentially aerogel.

Figure 9 shows the abundances of several elements relative to Si for six individual Mg- and Si-rich spots, of which three are displayed in Figs. 6a, 7e, and 7f. Next to Si and Mg, the main constituents are C and O, while other elements contribute only very little to the composition. For comparison, elemental abundances for three aerogel blanks analyzed by Stephan et al. (2008) are displayed in Fig. 9. They show that for all elements abundances relative to Si in aerogel much lower than observed for the Al foil regions.

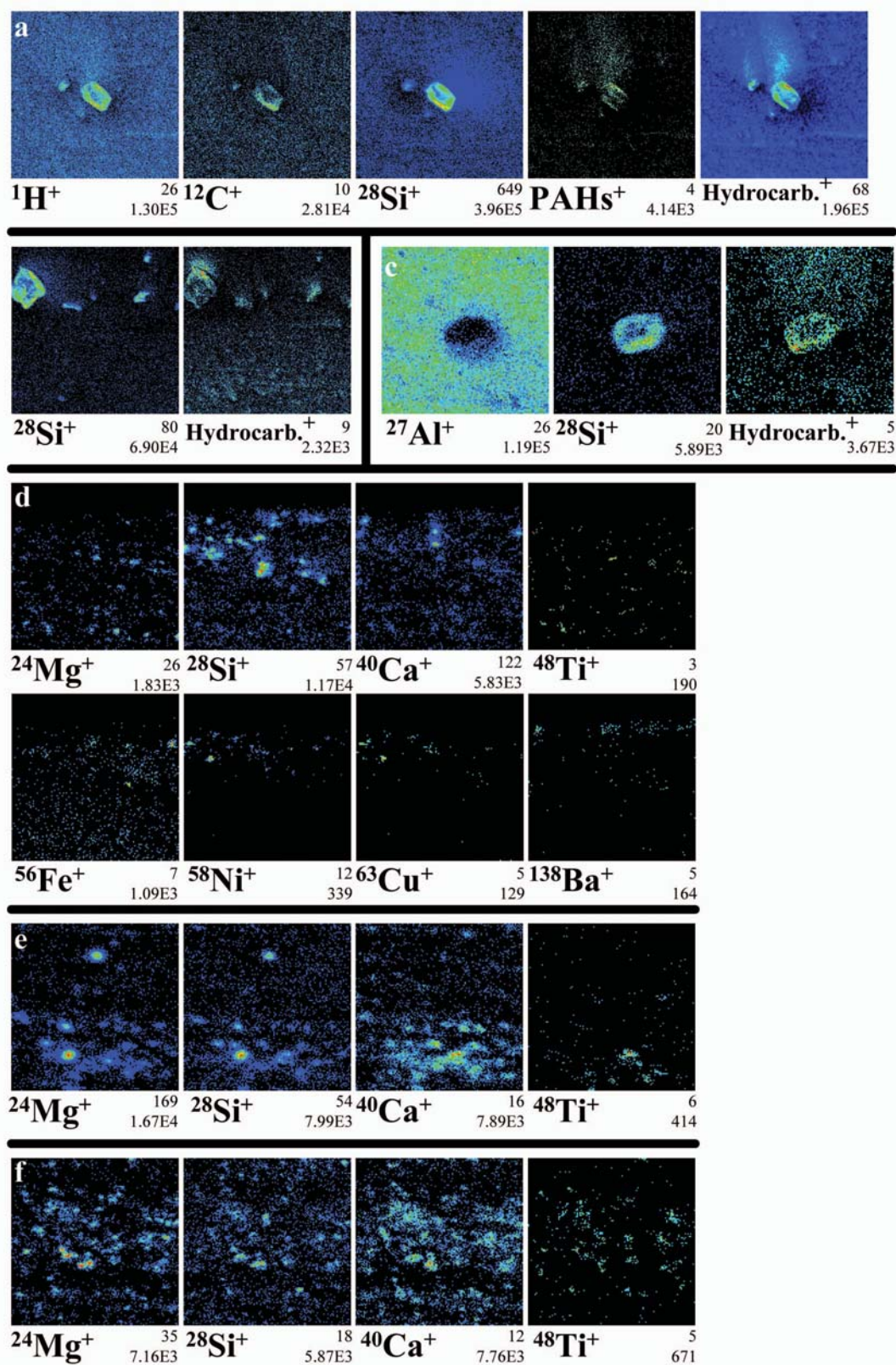


Fig. 7. Features (presumed contaminants) found on C2070W,1. a) Field of view is $78.8 \times 78.8 \mu\text{m}^2$. b) Field of view is $18.7 \times 18.7 \mu\text{m}^2$. c) Field of view is $101 \times 101 \mu\text{m}^2$. d) Field of view is $25.2 \times 25.2 \mu\text{m}^2$. e) Field of view is $30.8 \times 30.8 \mu\text{m}^2$. f) Field of view is $30.8 \times 30.8 \mu\text{m}^2$.

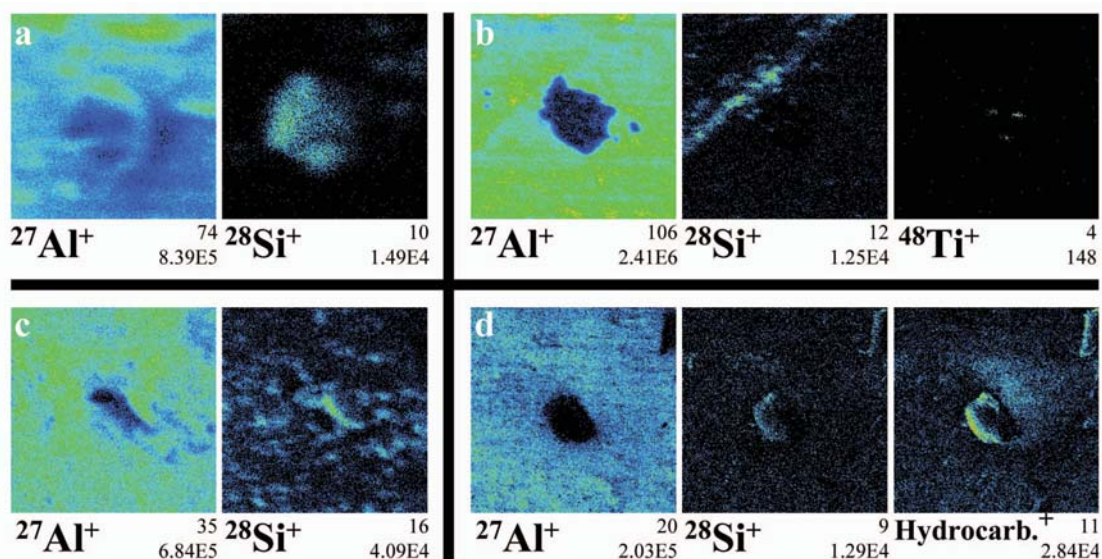


Fig. 8. Features (presumed contaminants) found on C2101W,1. a) Field of view is $9.7 \times 9.7 \mu\text{m}^2$. b) Field of view is $24.8 \times 24.8 \mu\text{m}^2$. c) Field of view is $25.3 \times 25.3 \mu\text{m}^2$. d) Field of view is $100 \times 100 \mu\text{m}^2$.

Figure 10 shows the element abundances relative to Si for five features whose compositions are dominated by Si, C, and O, and which also contain abundant hydrocarbons, as can be seen in Figs. 6b, 7a–c, and 8d.

Large Foil Craters

On six of the investigated foils, seven large impact craters between 50 and 240 μm in diameter were found and their residues were analyzed with TOF-SIMS. Secondary ion images for all craters are shown in Figs. 11–13. Quantitative results are summarized for the three main depressions of C2102N,1 #2 in Table 1 and for all analyzed crater residues in Fig. 14 as atomic element ratios relative to Si and normalized to CI ratios. Since only polymict crater residues are expected to comply with CI chondrite bulk composition, element abundances of monomineralic particles or impactors consisting of distinct mineral mixtures should substantially deviate from the CI abundance pattern. Element ratios relative to Si without CI normalization are summarized in Table 2.

C2009N,1

On this foil, one crater with a diameter of $\sim 64 \mu\text{m}$ was found. Here, residual matter within the crater rim was unambiguously identified (Fig. 11). No considerable element abundances were visible outside the crater. Element distribution in the residue on the crater rim is quite heterogeneous, so local hotspots for virtually all major constituents can be seen in the secondary ion images (Fig. 11). The lateral distributions of C, Na, Cl, K, Ti, Ni, and Cu are correlated, as well as the distributions of Mg, Si, S, Cr, Mn, and Fe. Calcium was not found above background in this residue.

The area of the crater rim rich in Ni and Cu shows virtually no correlation with other metal distributions, especially not with Fe, and was excluded for the definition of the region of interest to determine the elemental composition of the residue. Ni and Cu show elemental ratios that are much higher than observed in CI chondrites: Ni/Si is $\sim 26\times$ CI, Cu/Si even higher, $\sim 840\times$ CI, so these components are most likely contaminants from the Al foil.

Most of the major elements in this residue are within a factor of two CI chondritic; only Li and K have slightly higher abundances compared to CI together with modest depletions in Fe and Co.

The absence of Ca and the $(\text{Mg} + \text{Fe})/\text{Si}$ ratio of ~ 1 with a Fe/Mg ratio of ~ 0.3 (cf. Table 2) suggest that this cometary particle was dominated by a Mg-rich pyroxene-like composition.

C2029W,1

The large crater on this foil, measuring approximately $160 \mu\text{m} \times 120 \mu\text{m}$ in size, has an irregular shape. It is most likely the result of an aggregate impact, since several circular sub-areas are discernible in Fig. 1b and Fig. 11. Because of the rough topography of the sample area, only a part of the residue was initially accessible for TOF-SIMS investigation. Therefore, the sample was rotated by 180° following the first measurement and analyzed again (Fig. 11). In the second analysis, some areas that were not accessible during the first investigation were reached by the primary ion beam.

In Fig. 11, H^- , C^- , CH^- , and OH^- -rich spots in the rim area are visible. These spots are not directly connected with any other major constituents of the residue, but seem to be located in regions devoid of other atomic species.

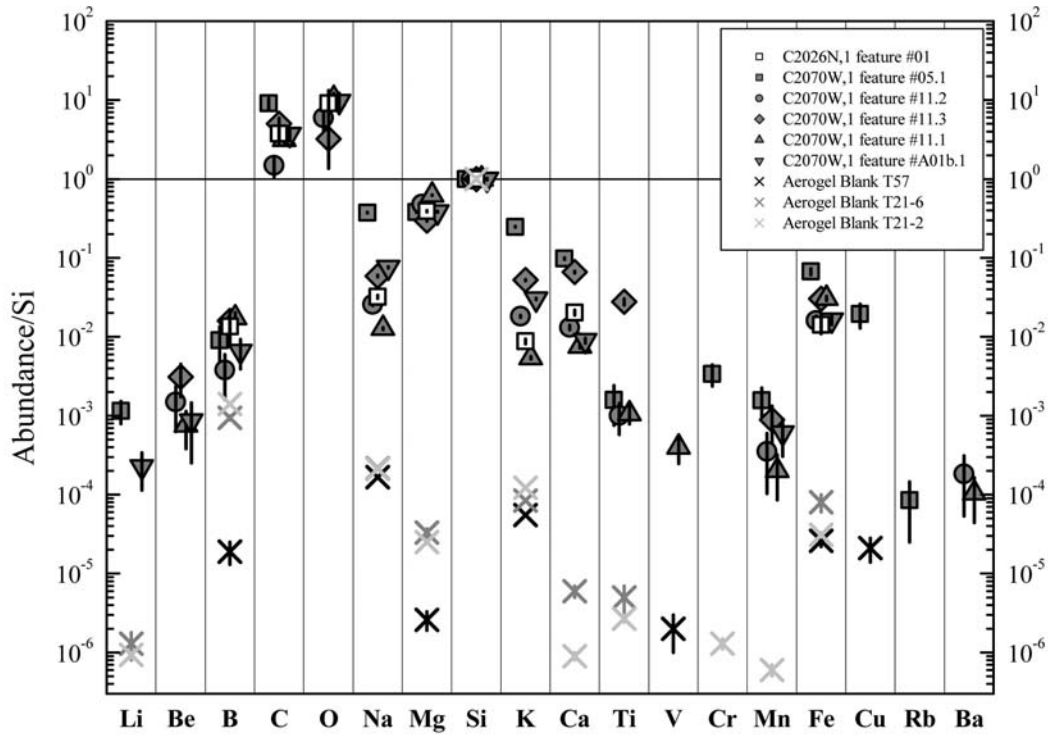


Fig. 9. Elemental abundances normalized to Si of Mg- and Si-rich spots found on foils C2026N,1 and C2070W,1. For comparison, elemental abundances for three aerogel blanks analyzed by Stephan et al. (2008) are displayed.

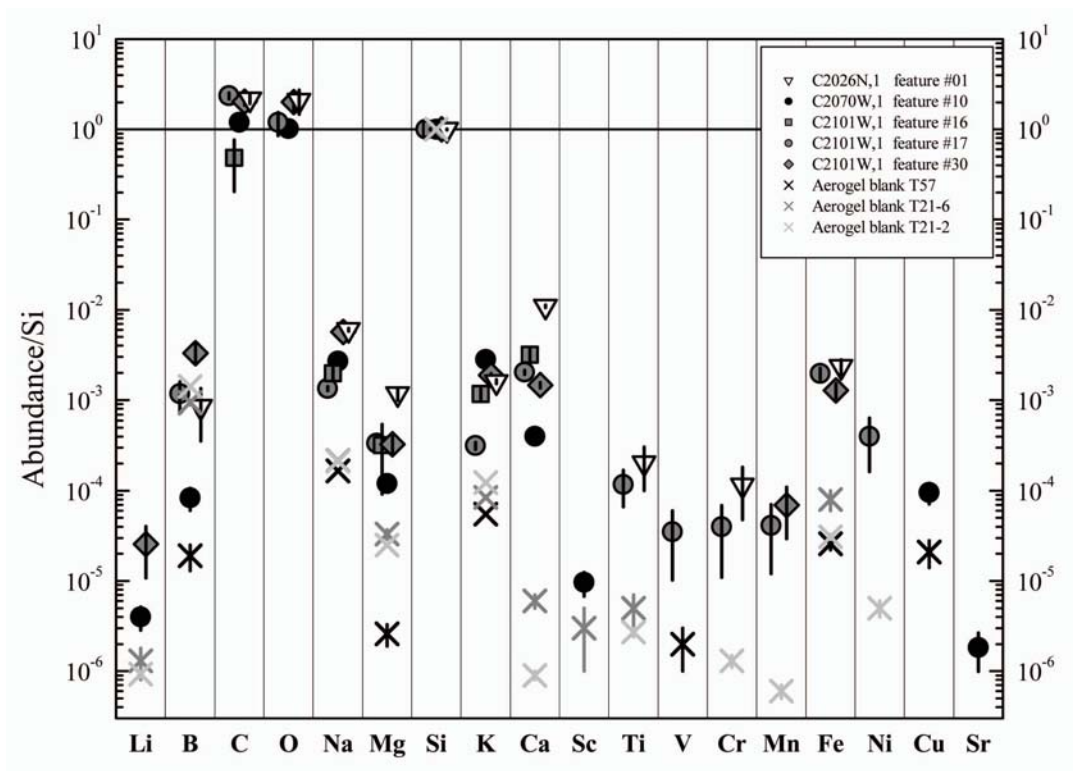


Fig. 10. Elemental abundances relative to Si are shown for five Si-rich features (probably aerogel debris), as well as abundances for three aerogel blanks.

Residue material is visible on the right side of the crater (Fig. 11, C2029W,1–0°), containing O, Na, Mg, Si, S, K, Ca, Fe, and Ni. The Si abundance in this residue is very low, so the inferred element ratios displayed in Fig. 14 show large deviations from CI. Na and Mg show high abundances relative to Si (Table 2), while Fe is in the same order of magnitude as Si and correlates laterally with S in the residue (Fig. 11).

After rotating the sample, another patch of residue was visible on the right side of the crater (Fig. 11). Also, the residual matter of this patch contains only very little Si, while O, Na, Mg, S, K, Ca, and Fe are comparable to the residue analyzed before sample rotation.

The comparably low abundance of Si indicates that the residue in the rim of this crater has no silicate composition. Furthermore, the well-correlated lateral distributions of S and Fe suggest that part of the impactor consisted of iron sulfide, although the S abundance cannot be quantified by TOF-SIMS, since S forms predominately negative secondary ions that cannot be related directly to Fe that forms only positive secondary ions.

C2086N,1

A crater with a diameter of ~59 μm was found in this foil. Residual matter was concentrated in the upper right quadrant of the impact crater, containing abundant O, Na, Mg, Si, S, Cl, K, Ti, Cr, Mn, and Fe, while virtually no Ca was found (Fig. 12; Table 2).

Abundances of almost all elements (Fig. 14) are near bulk CI values, only Mn and Fe are depleted by factors of 10 and 30, respectively. Ca was not found in the residue. This composition indicates that the particle is dominated by Mg-rich minerals like enstatite and forsterite, since the Mg/Si ratio is ~1.2 (Table 2).

C2086W,1

This foil contained one crater with a diameter of ~240 μm; the projectile was large enough to completely penetrate the foil. From the secondary ion images, residual material in the “southwestern” and “southern” region of the crater in Fig. 12 can be recognized. The compositional heterogeneity of the surrounding Al foil is especially evident in the distributions of Si, K, Ca, Ti, and Mn (Fig. 12). The large patch of residue in the lower right quadrant of Fig. 12 (C2086W,1–0°) contains C, O, Na, Mg, Si, Ca, Sc, Mn, and Fe, while the spot in the “south” consists of O, Mg, Si, S, Cl, Ca, Sc, Mn, and Fe. This spot is the location where Stadermann et al. (2008) reported a presolar grain.

Because of the size of the crater, a second analysis was performed after rotating the sample for 180° to investigate parts of the crater rim that were not accessible during the first measurement. While the region containing the residual

material that was located in the “southwest” before rotating the crater is not visible any more, a second patch of residue becomes visible after rotation in the upper right quadrant of Fig. 12 (C2086W,1–180°). The cometary material contains abundant C, O, Na, Mg, Si, S, Cl, K, Ca, and Fe as well as traces of Ti and Mn.

Na abundance is considerably high in all residual patches, as well as K in the residue accessible after sample rotation. Li, Ca, Sc, Ti, and Mn show concentrations relative to Si within a factor of 2 of bulk CI composition. Mg and Fe, however, are slightly depleted in all residues showing relative abundances of ~0.4× CI, while Ni is even lower (~0.2× CI).

C2091N,1

The large crater on this foil has a diameter of ~60 μm and unambiguously identifiable residual material at the right side of the crater rim (Fig. 13). The foil area in the vicinity of the crater shows high abundances of Si, K, Ca, Cr, Mn, and Fe, all heterogeneously distributed. The residue is rich in Na, Mg, and Si and has a considerable amount of Fe (Table 2) and S. Furthermore, traces of Li, K, Sc, Cr, Co, and Ni are found, while Ca and Ti have no clear connection to the crater rim. This is also the case for Mn; though a reasonably high signal intensity (Fig. 13) is detected in the rim area. However, the Mn abundance in surrounding foil areas denies a clear connection of Mn with the residue after blank correction.

For this residue, too, the Na abundance is relatively high (Fig. 14; Table 2). Li, Mg, K, Sc, and Cr values are all well within 2–3× CI. Fe, Co, and Ni abundances relative to Si are factors of 2–10 lower than in CI carbonaceous chondrites.

The composition of this residue is similar to the one of C2009N,1, so a similar assumption may be made for this cometary particle, i.e., a considerable part of the impactor may have a pyroxene- or olivine-like structure.

C2102N,1

Two impact features were found on this foil; the first is a crater with a diameter of ~85 μm and a shape suggesting a non-spherical, possibly aggregate particle, the second is a multiple impact feature, most likely caused by an aggregate impactor.

Crater #1

At least two sub-regions are visible in the crater. A large area of residue is located in the lower right area of the crater, while another patch of material is located in the upper left part of the rim (Fig. 13).

The main residue has abundant O, Na, Mg, Si, S, Cl, K, and Ca, and lower concentrations of B, C, Cr, Mn, Fe, and Ni, while the residual spot at the upper left contains mainly

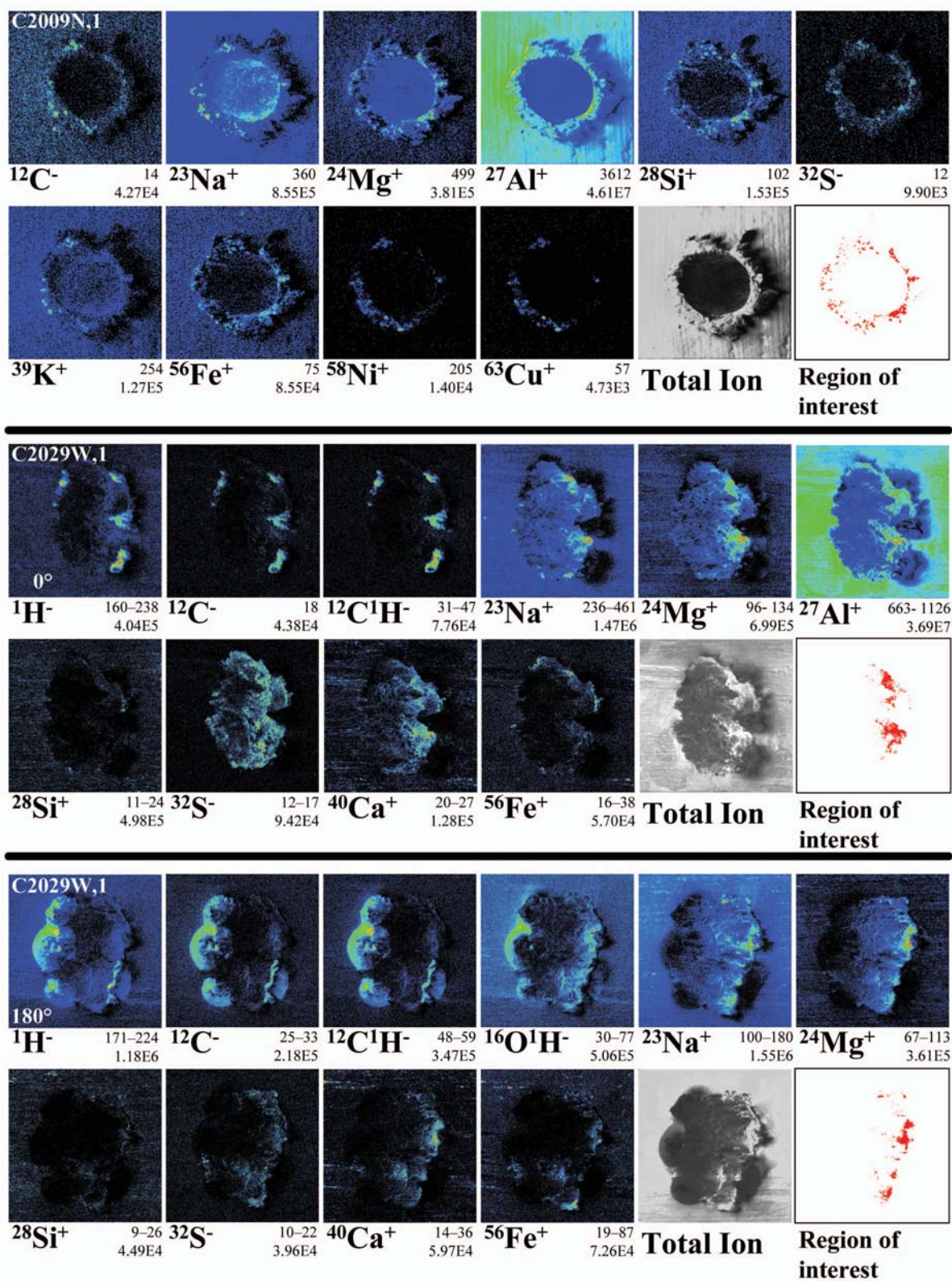


Fig. 11. Secondary ion images of the large craters on foils C2009N,1 and C2029W,1 (before and after sample rotation). In addition to the secondary ion images of the different species, a grayscale total positive secondary ion image is displayed for each crater, followed by the region of interest that was selected for the quantitative analysis of each residue. The fields of view are $120 \times 120 \mu\text{m}^2$, $199 \times 199 \mu\text{m}^2$, and $199 \times 199 \mu\text{m}^2$.

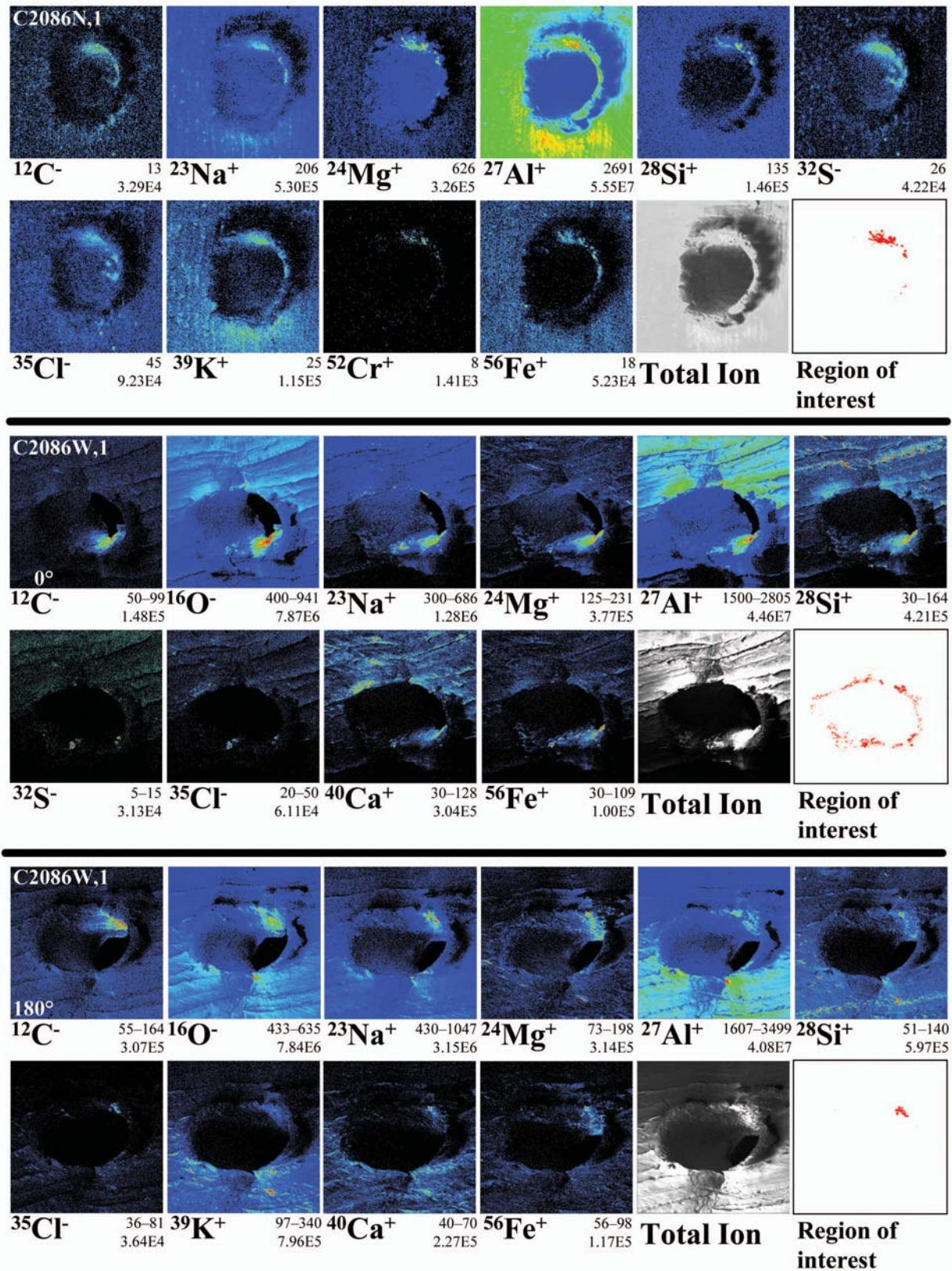


Fig. 12. Secondary ion images of the large craters on foils C2086N,1 and C2086W,1 (before and after sample rotation). The fields of view are $100 \times 100 \mu\text{m}^2$, $500 \times 500 \mu\text{m}^2$, and $500 \times 500 \mu\text{m}^2$.

C, O, Si, Ca, and Fe. Mg, Ca, Cr, and Mn have roughly solar abundances (Fig. 14), while Fe and Ni are depleted by factors of 6 and 3, respectively, in comparison to CI abundances. The alkali elements Li, Na, and K are 3–14× CI. The B, C, and O contents of the crater residues cannot be determined unambiguously, due to the heterogeneous distribution of these elements on the surrounding foil blank. Nevertheless, the ion images shown in Fig. 13 suggest that the residue material contains a finite amount of B and C above background. Additionally, S shows a strong presence in the main residue, although quantification for S is not possible, due to the lack of appropriate standards. The abundance pattern displayed in Fig. 14 is quite similar to bulk CI composition for the major constituents of the residue, so the cometary particle is most likely a mixture of different components. Furthermore, the observed (Mg + Fe)/Si ratio of ~1.55 suggests a mixture of high-Mg olivine- and pyroxene-like material as main components.

Crater #2

The second impact feature consists of at least three major sub-craters with diameters between 16 and 19 μm and possibly several smaller ones. Therefore, it has a much more complex distribution of elements than crater #1, as can be seen in Fig. 13. For better orientation, the three main depressions are referred to as #2.1, #2.2, and #2.3, advancing from top to the bottom of the area displayed in the secondary ion images in Fig. 13.

There are high levels of Na and S in depression #2.1, and Mg, K, Ca, Sc, and Fe show also comparably high abundances here (Table 1; Fig. 13). Mn has a solar-like abundance in this sub-area, while Cr, Co and Ni are 0.5–0.75× CI chondritic values.

Depression #2.2 also has relatively high Na and K abundances of 15 respectively 10× CI chondritic composition. Mg and Ca abundances are also above solar system values in this subcrater, but not as high as in #2.1. Cr, Mn, and Fe are all slightly below CI chondritic values, while Co and Ni have abundances of roughly 2× solar system composition. When compared to #2.1, the Fe/Co and Fe/Ni ratios are nearly inverted.

In the area of #2.3, the Na- and K ratios are lower than in the two other sub-craters, but still above solar system average by factors of 6–10. Mg, Ca, Ti, Cr, Mn, and Ni, however, are within a factor of 2 of CI chondritic values, whereas Fe and Co are depleted by factors from 2.5 to 3.

Despite the variations in element abundances between the three main depressions of C2102N,1 #2, the “bulk” composition displayed in the last column of Table 1 displays abundances within 2× solar system values for the majority of the elements. Larger deviations occur only for Na, K, Ca and Sc (Table 1; Fig. 14).

The different (Mg + Fe)/Si ratios of the three main areas suggest a polymict composition of the particle. #2.1 displays a ratio of ~4.5, indicating a mainly non-silicate nature of the residue in the crater rim.

Depression #2.2 has a (Mg + Fe)/Si ratio of 1.9, so the residual matter is presumably dominated by olivine-like silicates.

In the rim area of crater #2.3, the ratio is 1.45, pointing towards a mixture of olivine- and pyroxene-like silicates for the material of this residue, similar to what is observed for the residual matter in the rim of C2091N,1.

Bulk Element Composition

In Fig. 14, element ratios relative to CI chondritic composition and normalized to Si for all seven analyzed impact residues are shown. The abundances of individual crater residues show a wide variation. This scattering is probably due to a monomineralic nature of several particles captured on the Al foils. No single mineral has a CI-like composition. Therefore, particles that show a good agreement with CI abundances must represent a mixture of different minerals. Additionally, geometric means for the elements ratios are shown. For samples that were measured before and after rotation, geometric means for these two data sets were calculated as representative values for the “bulk” residues of the respective foil craters. These data were then used for the calculation of the overall geometric mean. Geometric means were selected because arithmetic averaging of element ratios easily produces meaningless numbers since relatively high ratios would dominate the averages. For the craters that were analyzed before and after rotation (C2029W,1 and C2086W,1), an average composition was taken before calculating the overall geometric mean shown in Fig. 14, since during every measurement different areas of residue were visible. Minor compositional differences between the two sets of measurements derive clearly from the heterogeneity of the impactor and affect mostly minor components. The large variations for the elemental composition of the residues from crater C2029W,1 are caused by variations in the overall low Si abundance (Fig. 11), which have a stronger influence on the element-to-silicon ratios than in cases where Si is a main constituent.

But despite the rather large deviations of individual abundances from CI values, the geometric means of half of the element ratios shown in Fig. 14 are within a factor of two of CI carbonaceous chondrite composition. Only for Na and Fe, the element ratios deviate more than a factor of four from CI values. Table 2 summarizes the atomic abundances normalized to Si of the seven analyzed crater residues. In contrast to investigations of high-velocity impact crater residues from the LDEF experiment, where element fractionation clearly occurred (Lange et al. 1986), no such effect was unambiguously observed.

Iron shows only moderate abundances in the residues, but Fe/Mg ratios range from ~1 to 0.027 (Table 2) and indicate therefore a wide range of silicate compositions.

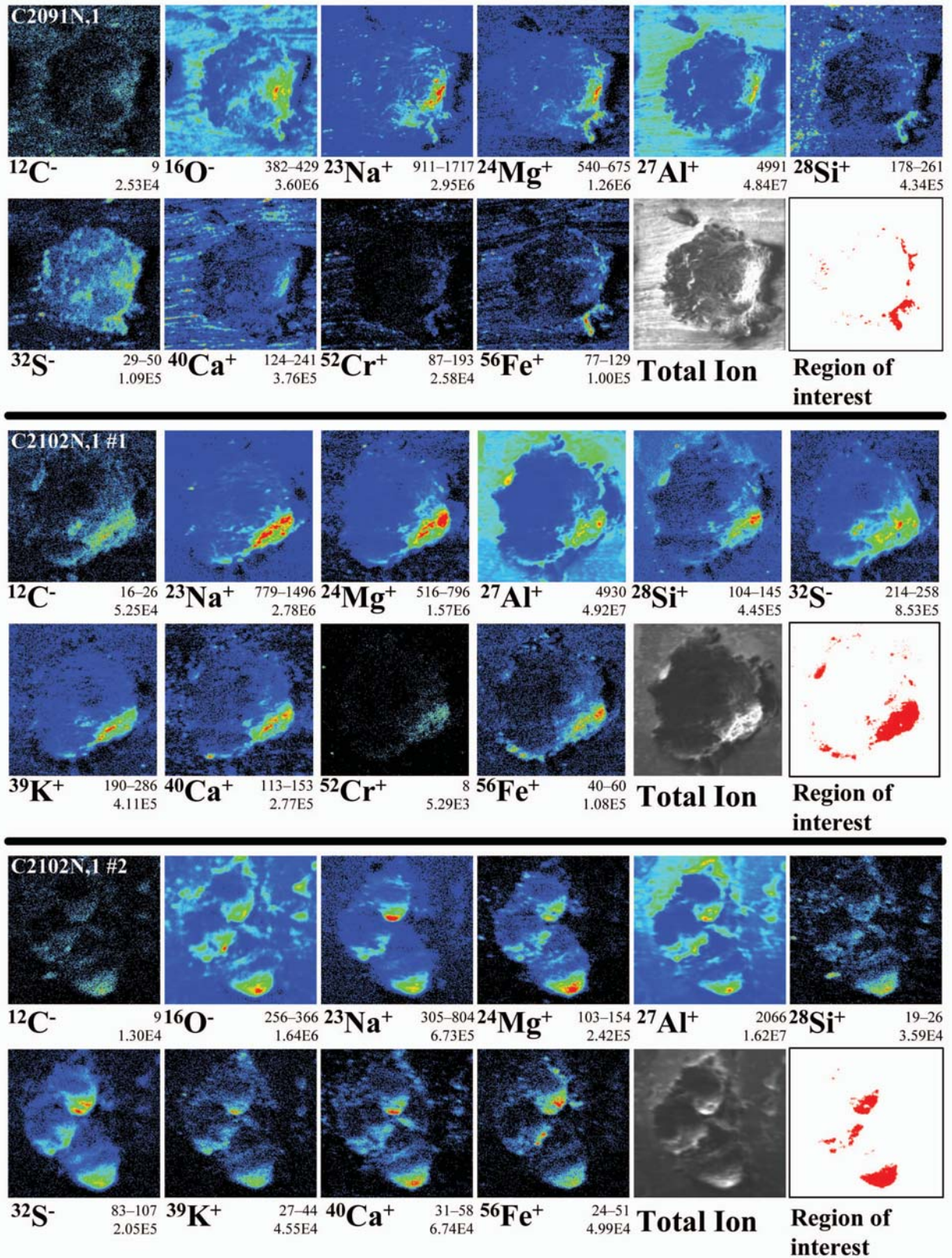


Fig. 13. Secondary ion images of the large craters on foils C2091N,1 and C2102N,1. The fields of view are $98 \times 98 \mu\text{m}^2$, $115 \times 118 \mu\text{m}^2$, and $55 \times 56 \mu\text{m}^2$.

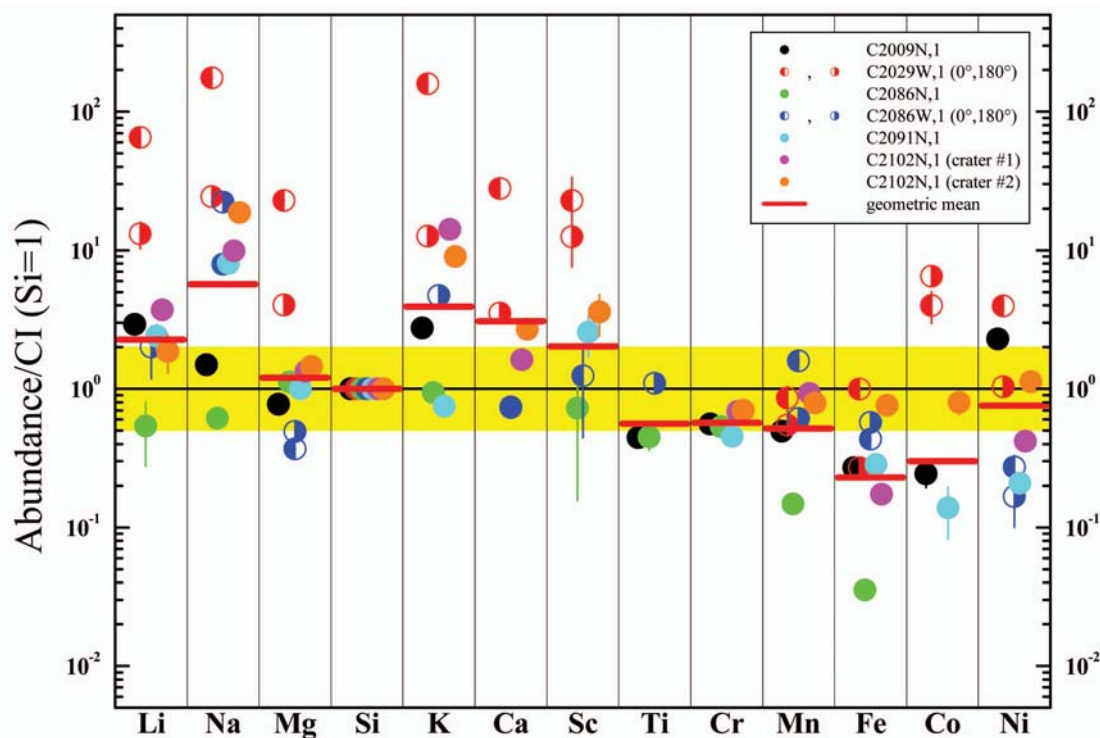


Fig. 14. Element ratios normalized to Si and CI for all seven crater residues analyzed. Data points between $0.5 \times$ CI and $2 \times$ CI abundances plot within the yellow area.

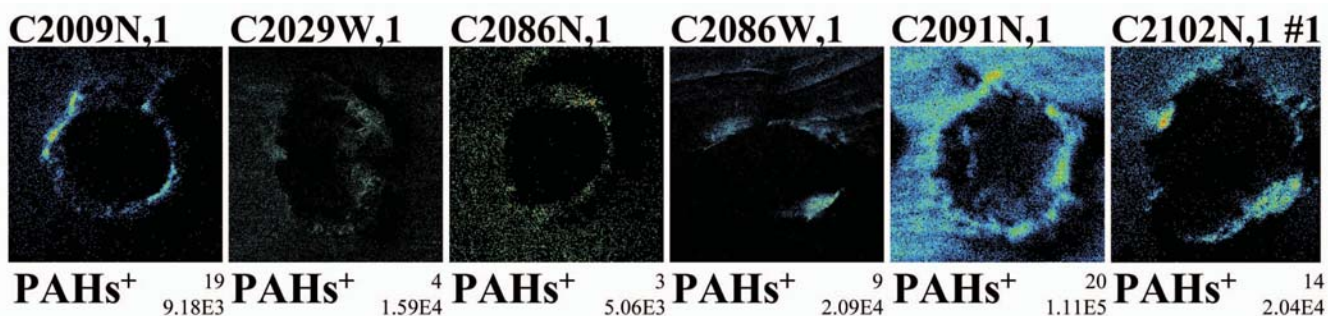


Fig. 15. Secondary ion images showing sum intensities of PAHs found in 6 crater residues. All secondary ion intensities for typical PAH masses between 115 u and 302 u are added. From the mass spectra for each sample that all look like the one shown in Fig. 16, it could be unambiguously shown that these mass peaks indeed result from PAHs.

Organic Material

Traces of complex organic matter, so-called polycyclic aromatic hydrocarbons (PAHs), which are present in primitive meteorites and interplanetary dust particles (IDPs) (Allamandola et al. 1987; Clemett et al. 1993; Messenger et al. 1998), were also found in six of the seven analyzed residues (Fig. 15). A typical PAH secondary ion mass spectrum is shown in Fig. 16. Displayed is the mass range that contains the dominant peaks of PAHs and PAH fragments in the cometary crater residues. The mass distribution of PAHs in TOF-SIMS spectra from cometary residues show significant differences from those of cometary matter in aerogel tracks

analyzed by two-step laser desorption laser ionization mass spectrometry (L^2MS) published by Sandford et al. (2006). For example, polyaromatic radicals like $C_9H_7^+$ and $C_{13}H_9^+$ are abundant in TOF-SIMS spectra (Fig. 16), while they are not present at all in L^2MS analyses. Furthermore, species like $C_{10}H_8^+$ and $C_{14}H_{10}^+$ that are observed with both techniques show different intensity patterns. These differences are due to the differing ionization processes of the applied techniques.

Since PAHs are nearly omnipresent in nature (Allamandola 1996), it was not initially clear if the observed molecules are indigenous to the residual matter or terrestrial contaminants.

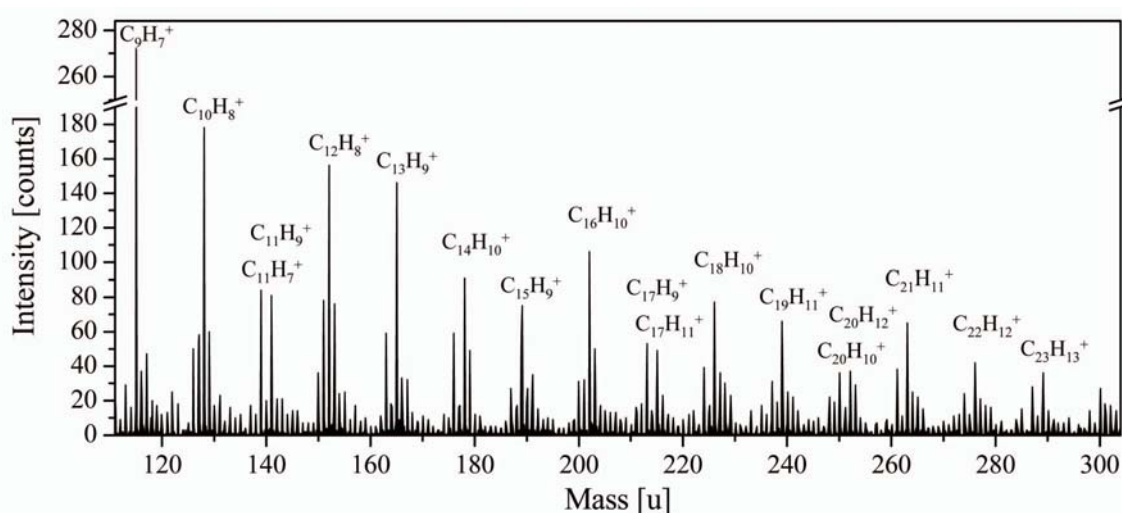


Fig. 16. Part of a TOF-SIMS mass spectrum of the crater residue C2009N,1 with sum formulae given for the major peaks. Relative maxima display typically mass differences of 11 or 13 u. In addition, there are often several peaks present that are separated by a mass difference corresponding to the mass of H₂.

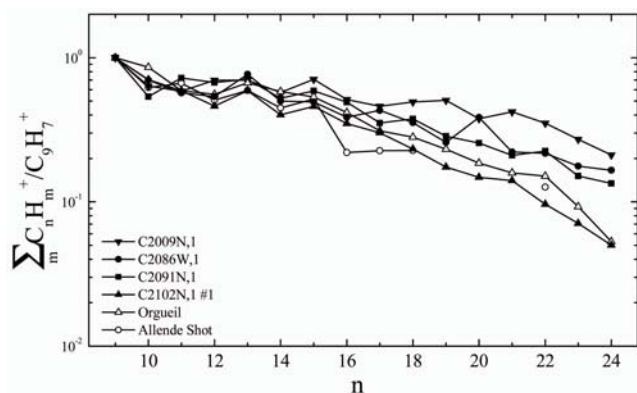


Fig. 17. Comparison of PAH signal intensities from four crater residues as discussed in the text with data from the CI carbonaceous chondrite Orgueil and material from an Allende test shot. The diagram shows the relative intensities of PAHs as a function of the number of carbon atoms relative to the intensity of C₉H₇⁺.

The craters on foils C2029W,1 and C2086N,1 show only very low sum intensities for PAHs in the mass range from 115 u to 302 u, and the PAH signal from the surrounding foil blank is about equal in intensity. It is therefore likely that these PAHs are largely contamination, and the following discussion will focus only on those crater residues with reasonably high PAH intensities above background.

Figure 17 shows the relative abundances of different PAHs with varying number of C atoms found in the secondary ion spectra of these craters. For comparison, the relative abundances of material from the meteorite Orgueil as well as residual matter from an Allende projectile shot onto Al foil at 6.1 km s⁻¹ are displayed (Stephan et al. 2005; Hoppe et al. 2006). The PAHs in the analyzed crater residues on the foils C2009N,1, C2086W,1, and C2091N,1 show a much less steep decrease in abundance with increasing

number of carbon atoms than Orgueil (Stephan et al. 2003; Sandford et al. 2006). Even PAHs in the crater residue of the Allende test shot do not show an abundance pattern similar to these cometary crater residues. The residual matter of crater #1 on C2102N,1, in contrast, shows a steep decrease comparable to that of Orgueil.

Although C2091N,1 has a comparably strong background signal of PAHs (see Fig. 15), the pattern of abundances displayed in Fig. 17 is very similar to the patterns of C2086W,1 and C2091N,1, which have no significant abundance of PAHs outside the crater residue.

Generally, the decrease of PAHs with increasing carbon number is less pronounced (Fig. 17) than it is for terrestrial samples and even for PAHs from primitive meteorites (Stephan et al. 2003). Thus, the cometary residues contain relatively more “heavier” PAH molecules than other extraterrestrial and terrestrial samples investigated so far.

Since complex molecules are easily fragmented and destroyed during the necessary sputter cleaning process, all data for the PAHs were obtained from TOF-SIMS analyses performed prior to sputter cleaning.

DISCUSSION

Foils without Large Craters—C2026N,1, C2070W,1, and C2101W,1

The Si-features with associated hydrocarbons are most likely fine-grained aerogel debris that clings to the aluminum foils (Figs. 6, 7, and 8). Aerogel pieces of different sizes located on the Al foils were clearly identifiable under the optical microscope, and features equivalent to those displayed in Figs. 6a and 6b were seen in the aerogel-contaminated foil areas. The Si-rich features found there

contain C and O as main constituents (Figs. 7, 8a, and 10), which is consistent with preflight analyses of the silica aerogel (Sandford et al. 2006). Comparison with three aerogel blanks from Stephan et al. (2008) shows that these features are not pristine aerogel, since their trace element contents are higher than observed for the blanks. However, since their main components are Si, C, and O and the trace element pattern shows some similarity to unprocessed aerogel, these features were identified as aerogel-like debris.

The origin of the spots displaying correlated Mg and Si abundances is unknown; but their non-chondritic composition suggests that they are some kind of contamination (Fig. 9). These spots contain also C and O, and a much higher level of minor constituents than the three aerogel blanks displayed in Fig. 9. However, their high C, O, and Si content proposes that they are possibly processed, perhaps melted, aerogel that was relocated on the aluminum foils after particle impacts in the neighboring aerogel tiles. On the other hand, it presently cannot be excluded that they are a metallurgical contaminant of the Al foils, as are other elemental hotspots, containing Cr, Mn, Fe, Ni, Cu, Ba, and Tl. A wide range of minor and trace element contents have been reported from within the flown Stardust foils (Kearsley et al. 2006, 2007), and as these can be shown to occur on non-exposed surfaces, and are not spatially associated with crater-like structures, these are presumably impurities inherent in the foils. Similar features occurred on the Al-1100-foils used in laboratory experiments (Hoppe et al. 2006; Kearsley et al. 2006; Leitner et al. 2006a, 2006b). Therefore, an extraterrestrial origin of these contaminants can be excluded.

The origin of the Tl content of the spot shown in Fig. 6b is not clear so far. Tl atoms can substitute alkali atoms like Na or K in compounds, since they have similar chemical properties, so it cannot be deduced if this Tl spot is a metallurgical impurity indigenous to the Al foil, or if it is part of one of the observed surface contaminants that contain alkalis.

Debris resembling aerogel is found frequently on the foils, as well as Mg-Si spots, Ti spots, and areas containing Ca and CaO. Furthermore, features containing alkalis occur regularly, and spots containing Cr, Mn, and Fe are observed casually. But even more rarely occurring contaminations have to be considered for data interpretation as is demonstrated by the crater on foil C2009N,1, where one Ni-Cu inclusion was hit by a cometary particle. Although the Tl-rich spot discovered on foil C2026N,1 is the only one discovered in this investigation, analyses on some of the test foils revealed a certain Tl background in some foil areas.

Large Foil Craters

The impact residues investigated on the foils exhibit, at a first glance, a wide range of element abundances. This is

probably due to the fact that not only polymict particles were captured on the aluminum foils, but also compounds of few minerals or even nearly monomineralic grains that cannot show CI-like compositions, since no mineral with CI chondritic element abundances exists. This explains the wide scatter of abundances relative to Si and bulk CI composition observed in the crater residues.

In addition, the observed high abundances of some elements relative to Si and bulk CI values may be due to the effect already observed during the analysis of mineral standards. There, higher abundances than predicted from literature data and reference SEM-EDX analyses were observed especially for relatively volatile species like Na and K, but only where these elements are minor constituents or even trace elements in the analyzed materials (Fig. 4), i.e., the mobilization seems predominately to affect volatile elements with low initial relative abundances.

When considering the mineralogy of the residual matter in the investigated impact craters, there are two different groups of particles apparent on the foils. The first group consists of particles that are nearly monomineralic or contain few distinct minerals, and so show quite large deviations from bulk CI chondritic abundances (Fig. 14).

A large scattering of data points is observed for the residue of the aggregate crater C2029W,1 that suggests a composition that is clearly non-silicate but contains iron sulfide (Fig. 11; Table 2). For investigations analyzing the residual matter at the crater bottom, a silicate-like composition of the impactor was reported (Zolensky et al. 2006). Thus, the low Si abundance observed in this study in the crater rim emphasizes the complex and heterogeneous structure of this impact feature. The main part of the silicates in this residue, as reported by Kearsley et al. (2008) was not accessible by TOF-SIMS analysis and does not contribute to the elemental composition of the rim residue, generating the discrepancy between the TOF-SIMS and SEM-EDX results.

The particles creating the circular craters C2009N,1 and C2091N,1 show similar abundance patterns that may indicate a largely pyroxene-like nature, with virtually no Ca and a (Mg + Fe)/Si ratio of ~1. The high abundances of Ni and Cu in a part of the crater rim of C2009N,1 are most likely caused by a Ni- and Cu-rich impurity indigenous to the foil. Evidence for such impurities was also found on foil C2070W,1, without any correlation to an existing crater (Fig. 7d).

Furthermore, the Ni/Cu ratio of the hotspots found on foil C2070W,1 (Fig. 7d) matches with the ratio determined for the rim area of the crater on C2009N,1 (~2.9 in both cases). Thus, it seems likely that a cometary particle creating the crater has hit one of the Ni-Cu impurities in the foils and has mixed with it partially while creating the crater.

C2086N,1 is another example for a mainly monomineralic particle. Mn and especially Fe are strongly

depleted in comparison to bulk CI chondritic values. The Mg/Si ratio of 1.2, together with the absence of Ca and the very low Fe abundance (Table 2) indicates a high-Mg silicate, similar to enstatite, or, as concluded by Kearsley et al. (2008), forsterite.

The second group contains those cometary particles, that display a composition quite similar to CI chondrites and which therefore are polymict compounds of different mineral phases. The residues of C2102N,1 #2 and C2086W,1 clearly are of this type; their major constituents are well in the range of bulk CI composition. The three sub-areas of C2102N,1 #2, however, show significant variations in their elemental composition and suggested mineralogy and emphasize the heterogeneous nature of the aggregate particle. C2102N,1 #1 has an Fe/Si ratio that is more similar to those observed for C2009N,1 and C2091N,1, but this residue has a generally more CI-like composition than the two other particles, therefore it is more likely to be classified as polymict.

The overall residue composition (Table 2) shows, besides Si, a comparably high level of Mg, together with moderately abundant Fe and generally low Ca abundances. This is consistent with Zolensky et al. (2006), where a wide range of olivine and low-Ca pyroxene compositions from the cometary grains are reported, together with several alkali-rich mineral phases. However, the unusual high Na abundances observed in the majority of the residues do probably not reflect the true cometary composition, but are rather the result of mobilization of volatiles during foil impacts.

Organics

The seven investigated crater residues show a wide range of abundances of organic molecules. Apart from crater #2 on foil C2102N,1 which contained no complex organics at all, the six other residual craters have a PAH-bearing component. The origin and nature of these PAHs is not clear; terrestrial contamination has to be taken into account, but there are several indications for a non-terrestrial origin of the observed PAHs.

Especially the craters C2009N,1 and C2086W,1 show no significant abundance of PAHs in the neighborhood of the craters, making contamination of all crater areas with terrestrial organic matter unlikely. Furthermore, the very origin of the PAHs surrounding crater C2091N,1 is unknown; from their lateral distribution, it cannot be inferred if they are terrestrial contaminations or cometary matter deposited around the actual crater. So, a cometary origin of these PAHs cannot a priori be excluded.

Obviously, there exists a significant difference between the cometary organics and other primitive complex organic material, since the cometary residues contain proportionally more high-mass PAH molecules. This "enrichment" in heavy PAHs is either simply due to organic material containing

more heavy PAHs than were observed in other analyses, or it is caused by the preferential loss of low mass PAHs during impact on the foils (Stephan et al. 2003; Sandford et al. 2006). However, the latter explanation fails since during the Allende test shots a steeper decrease of PAH intensity with increasing mass was observed.

Additionally, the results from the analysis of crater #1 on C2102N,1 indicate the existence of another component of PAH-bearing material. This residue is obviously less "enriched" in heavier PAHs and thus, looks similar to PAHs found in primitive meteorites like Orgueil. Whether this comparably lower content of heavy PAHs is indigenous to the organic matter of the residue or not is still debatable.

CONCLUSIONS

This study clearly demonstrates that TOF-SIMS is suitable for the identification and analysis of cometary impact residues captured in aluminum foil. Moreover, since TOF-SIMS is virtually non-destructive, the samples are still available for other analytical techniques after TOF-SIMS investigation.

The determination of the elemental compositions of the seven investigated foil crater residues was complicated by impurities intrinsic to the Al-foil targets used on Stardust, as well as surface contaminations. Nevertheless, unambiguous identification and analysis of all investigated residues was possible.

The cometary matter in the impact craters displays a wide compositional span; nearly monomineralic grains, aggregates of non-silicate composition, as well as compact and aggregate particles of polymict compound were observed. However, Mg-rich, Ca-poor silicates are, together with Fe-Ni sulfides, a dominant component of the residue material.

Furthermore, minor elements show a wide variety of elemental ratios throughout the samples, so they seem to be quite heterogeneously distributed in the cometary material. This is consistent with observations made for primitive meteorites (Brownlee et al. 1984). However, the average element composition of the seven analyzed cometary residues is quite similar to bulk CI-chondritic values.

Complex organic molecules like PAHs are present in most cometary particles captured on Stardust aluminum foil. The larger fraction of these PAH-bearing materials is richer in heavier PAHs relative to $C_9H_7^+$ than other extraterrestrial and also terrestrial samples. This is either due to a higher abundance of heavy PAHs in the cometary particles, or to preferential fractionation of low-mass molecules during the impact.

A smaller fraction of the PAH-bearing material does not display these relative high abundances in heavier PAH-components and resembles material from primitive meteorites or even terrestrial material. This similarity is either

indigenous to the organic matter of the particle or an indicator for structural differences of the PAHs contained in the impactor and thus a different fragmentation behavior during the impact.

The TOF-SIMS investigation of elements as well as of organic compounds in the investigated crater residues reveals a quite heterogeneous composition of cometary matter.

Acknowledgments—We thank Frank J. Stadermann of the Washington University in Saint Louis, Missouri, for straightening the aluminum foils prior to our analysis, Mark Burchell and Mike Cole of the University of Kent in Canterbury, UK, who kindly performed the light-gas gun experiments for the mineral standard powders, and the Natural History Museum, London for electron microscopy facilities. This work was supported by the Deutsche Forschungsgemeinschaft through grant STE 576/17-1. The manuscript benefited from thorough reviews by Frank J. Stadermann, Peter Hoppe, and the associate editor Ian Lyon. The Stardust mission to comet 81P/Wild 2 was sponsored by NASA and executed jointly by the Jet Propulsion Laboratory and Lockheed Martin Space Systems. We are greatly indebted to many individuals who assured a successful comet encounter and who safely returned to Earth the Stardust collectors and its samples.

Editorial Handling—Dr. Ian Lyon

REFERENCES

- Allamandola L. J. 1996. PAHs, they're everywhere! In *The cosmic dust connection*, edited by Greenberg J. M. Dordrecht: Kluwer Academic Publishers. pp. 81–102.
- Allamandola L. J., Sandford S. A., and Wopenka B. 1987. Interstellar polycyclic aromatic hydrocarbons and carbons in interplanetary dust particles and meteorites. *Science* 237:56–59.
- Amari S., Foote J., Simon C., Swan P., Walker R. M., Zinner E., Jessberger E. K., Lange G., and Stadermann F. 1991. SIMS chemical analysis of extended impact features from the trailing edge portion of experiment A0187-2. In *LDEF—69 Months in Space—First LDEF Post-Retrieval Symposium*, edited by Levine A. S. NASA Conference Publication #3134, Washington, D.C.: NASA. pp. 503–516.
- Anders E. and Grevesse N. 1989. Abundances of the elements: Meteoritic and solar. *Geochimica et Cosmochimica Acta* 53:197–214.
- Brownlee D. E., Tsou P., Anderson J. D., Hanner M. S., Newburn R. L., Sekanina Z., Clark B. C., Hörz F., Zolensky M. E., Kissel J., McDonnell J. A. M., Sandford S. A., and Tuzzolino A. J. 2003. Stardust: Comet and interstellar dust sample return mission. *Journal of Geophysical Research* 108:E8111.
- Brownlee D. E., Wheelock M. M., and Bradley J. P. 1984. Point count analysis of interplanetary dust and fine-grained meteoritic materials (abstract). 15th Lunar and Planetary Science Conference. pp. 94–95.
- Clemett S. J., Maechling C. R., Zare R. N., Swan P. D., and Walker R. M. 1993. Identification of complex aromatic molecules in individual interplanetary dust particles. *Science* 262:721–725.
- Hoppe P., Stadermann F. J., Stephan T., Floss C., Leitner J., Marhas K. K., and Hörz F. 2006. SIMS studies of Allende projectiles fired into Stardust-type aluminum foils at 6 km/sec. *Meteoritics & Planetary Science* 41:197–209.
- Hörz F., Bastien R., Borg J., Bradley J. P., Bridges J. C., Brownlee D. E., Burchell M. J., Chi M., Cintala M. J., Dai Z. R., Djouadi Z., Dominguez G., Economou T. E., Faïrey S. A. J., Floss C., Franchi I. A., Graham G. A., Green S. F., Heck P., Hoppe P., Huth J., Ishii H., Kearsley A. T., Kissel J., Leitner J., Leroux H., Marhas K., Messenger K., Schwandt C. S., See T. H., Snead C., Stadermann F. J., Stephan T., Stroud R., Teslich N., Trigo-Rodríguez J. M., Tuzzolino A. J., Troadec D., Tsou P., Warren J., Westphal A., Wozniakiewicz P., Wright I., and Zinner E. 2006. Impact features on Stardust: Implications for comet 81P/Wild 2 dust. *Science* 314:1716–1719.
- Hörz F., Fechtig H., Janicke J., and Schneider E. 1983. Morphology and chemistry of projectile residue in small experimental impact craters. *Journal of Geophysical Research* 88:B353–B363.
- Kearsley A. T., Burchell M. J., Hörz F., Cole M. J., and Schwandt C. S. 2006. Laboratory simulation of impacts on aluminum foils of the Stardust spacecraft: Calibration of dust particle size from comet Wild 2. *Meteoritics & Planetary Science* 41:167–180.
- Kearsley A. T., Graham G. A., Burchell M. J., Cole M. J., Dai Z. R., Teslich N., Bradley J. P., Chater R., Wozniakiewicz P. A., Spratt J., and Jones G. 2007. Analytical scanning and transmission electron microscopy of laboratory impacts on Stardust aluminum foils: Interpreting impact crater morphology and the composition of impact residues. *Meteoritics & Planetary Science* 42:191–210.
- Kearsley A. T., Borg J., Graham G. A., Burchell M. J., Cole M. J., Leroux H., Bridges J. C., Hörz F., Wozniakiewicz P. J., Bland P. A., Bradley J. P., Dai Z. R., Teslich N., See T., Hoppe P., Heck P. R., Huth J., Stadermann F. J., Floss C., Marhas K., Stephan T., and Leitner J. 2008. Dust from comet Wild 2: Interpreting particle size, shape, structure, and composition from impact features on the Stardust aluminum foils. *Meteoritics & Planetary Science* 43. This issue.
- Lange G., Aigner S., Igenbergs E., Jessberger E. K., Kuczera H., Maas D., Sutton S., Weishaupt U., and Zinner E. 1986. Chemical fractionation effects during high-velocity impact. *Advances in Space Research* 6:9–12.
- Leitner J., Stephan T., and Hörz F. 2006a. TOF-SIMS analysis of residues of projectiles shot onto Stardust aluminum foil (abstract #1576). 37th Lunar and Planetary Science Conference. CD-ROM.
- Leitner J., Stephan T., Kearsley A. T., and Hörz F. 2006b. TOF-SIMS analysis of crater residues from projectiles shot onto aluminum foil (abstract). *Meteoritics & Planetary Science* 41:A105.
- Messenger S., Amari S., Gao X., Walker R. M., Clemett S. J., Chillier X. D. F., Zare R. N., and Lewis R. S. 1998. Indigenous polycyclic aromatic hydrocarbons in circumstellar graphite grains from primitive meteorites. *The Astrophysical Journal* 502:284–295.
- Rost D., Stephan T., and Jessberger E. K. 1999. Surface analysis of stratospheric dust particles. *Meteoritics & Planetary Science* 34:637–646.
- Sandford S. A., Aléon J., Alexander C. M. O'D., Araki T., Bajt S., Baratta G. A., Borg J., Bradley J. P., Brownlee D. E., Brucato J. R., Burchell M. J., Busemann H., Butterworth A., Clemett S. J., Cody G., Colangeli L., Cooper G., D'Hendecourt L., Djouadi Z., Dworkin J. P., Ferrini G., Fleckenstein H., Flynn G. J., Franchi I. A., Fries M., Gilles M. K., Glavin D. P., Gounelle M., Grossemy F., Jacobsen C., Keller L. P., Kilcoyne A. L. D., Leitner J., Matrajt G., Meibom A., Mennella V., Mostefaoui S., Nittler L. R., Palumbo M. E., Papanastassiou D. A., Robert F., Rotundi A., Snead C. J., Spencer M. K., Stadermann F. J., Steele A., Stephan T., Tsou P., Tyliszczak T., Westphal A. J., Wirick S., Wopenka B., Yabuta H., Zare R. N., and Zolensky M. E. 2006. Organics captured from comet 81P/Wild 2 by the Stardust spacecraft. *Science* 314:1720–1724.

- Stadermann F. J., Hoppe P., Floss C., Heck P. R., Hörz F., Huth J., Kearsley A. T., Leitner J., Marhas K. K., McKeegan K. D., and Stephan T. 2008. Stardust in Stardust—The C, N, and O isotopic compositions of Wild 2 cometary matter in Al foil impacts. *Meteoritics & Planetary Science* 43. This issue.
- Stephan T. 2001. TOF-SIMS in cosmochemistry. *Planetary and Space Science* 49:859–906.
- Stephan T., Jessberger E. K., Heiss C. H., and Rost D. 2003. TOF-SIMS analysis of polycyclic aromatic hydrocarbons in Allan Hills 84001. *Meteoritics & Planetary Science* 38:109–116.
- Stephan T., Leitner J., and Hörz F. 2005. TOF-SIMS analysis of residues from Allende projectiles shot onto aluminum foil—A Stardust dress rehearsal. In *Workshop on Dust in Planetary Systems*. LPI Contribution #1280. Houston: Lunar and Planetary Institute. pp. 136–137.
- Stephan T., Rost D., Vicenzi E. P., Bullock E. S., MacPherson G. J., Westphal A. J., Snead C. J., Flynn G. J., Sandford S. A., and Zolensky M. E. 2008. TOF-SIMS analysis of cometary matter in Stardust aerogel tracks. *Meteoritics & Planetary Science* 43. This issue.
- Tsou P., Brownlee D. E., Sandford S. A., Hörz F., and Zolensky M. E. 2003. Wild 2 and interstellar sample collection and Earth return. *Journal of Geophysical Research* 108:E8113.
- Zolensky M. E., Zega T. J., Yano H., Wirick S., Westphal A. J., Weisberg M. K., Weber I., Warren J. L., Velbel M. A., Tsuchiyama A., Tsou P., Toppani A., Tomioka N., Tomeoka K., Teslich N., Taheri M., Susini J., Stroud R., Stephan T., Stadermann F. J., Snead C. J., Simon S. B., Simionovici A., See T. H., Robert F., Rietmeijer F. J. M., Rao W., Perronnet M. C., Papanastassiou D. A., Okudaira K., Ohsumi K., Ohnishi I., Nakamura-Messenger K., Nakamura T., Mostefaoui S., Mikouchi T., Meibom A., Matrajt G., Marcus M. A., Leroux H., Lemelle L., Le L., Lanzirotti A., Langenhorst F., Krot A. N., Keller L. P., Kearsley A. T., Joswiak D., Jacob D., Ishii H., Harvey R., Hagiya K., Grossman L., Grossman J. N., Graham G. A., Gounelle M., Gillet Ph., Genge M. J., Flynn G., Ferroir T., Fallon S., Ebel D. S., Dai Z. R., Cordier P., Clark B., Chi M., Butterworth A. L., Brownlee D. E., Bridges J. C., Brennan S., Brearley A., Bradley J. P., Bleuet P., Bland P. A., and Bastien R. 2006. Mineralogy and petrology of comet 81P/Wild 2 nucleus samples. *Science* 314:1735–1739.

APPENDIX

In the following tables, element ratios for the analyzed crater residues before blank correction (“raw data”), for the foil blank surrounding the investigated crater (“Al blank”), and finally for the blank-corrected data (“corrected data”) are

shown. Data given in italics were discarded for evaluation, either because the blank signal was found to be higher than 50% of the entire signal (i.e., $(E/Al)_b > (E/Al)_r$), or after blank correction abundances below zero (or abundances with uncertainties >100%) were obtained. Statistical errors are given as last significant digit in parentheses.

C2009N,1

Element	Raw data (ions/Si ⁺)	Al blank (ions/Si ⁺ _{raw})	Corrected data (ions/Si ⁺)	Corrected data (abd./Si)
Li	0.0020(3)	0.000070(8)	0.0021(3)	0.00017(2)
Na	1.96(1)	0.2459(5)	1.87(1)	0.0854(4)
Mg	5.88(2)	0.0265(2)	6.39(2)	0.829(2)
Al	<i>32.71(3)</i>	<i>32.15(1)</i>	<i>0.61(4)</i>	<i>0.085(5)</i>
Si	1.000(9)	0.083(1)	1.00(1)	1.00(1)
K	0.408(4)	0.0585(3)	0.381(4)	0.0104(1)
Ca	<i>0.210(3)</i>	<i>0.1227(4)</i>	<i>0.095(3)</i>	<i>0.0069(2)</i>
Ti	0.0066(6)	0.0009(2)	0.0062(7)	0.0011(1)
Cr	0.036(1)	0.00028(2)	0.039(1)	0.0075(2)
Mn	0.0198(8)	0.00118(4)	0.020(1)	0.0047(2)
Fe	0.57(2)	0.043(1)	0.57(2)	0.24(1)
Co	0.0008(2)	0.000017(6)	0.0008(2)	0.0006(1)
Ni	0.098(2)	0.00024(5)	0.107(3)	0.113(3)

C2029W,1 (0°)

Element	Raw data (ions/Si ⁺)	Al blank (ions/Si ⁺ _{raw})	Corrected data (ions/Si ⁺)	Corrected data (abd./Si)
Li	0.022(3)	0.0015(1)	0.05(1)	0.0037(5)
Na	100.6(2)	5.89(1)	219.6(4)	10.04(2)
Mg	83.6(2)	2.22(1)	188.7(4)	24.49(6)
Al	406.7(4)	406.4(1)	0.6(9)	0.08(12)
Si	1.00(3)	0.569(8)	1.00(7)	1.00(7)
K	10.55(6)	1.009(4)	22.1(1)	0.601(4)
Ca	10.51(6)	0.460(3)	23.3(1)	1.71(1)
Sc	0.003(1)	0.0008(1)	0.005(2)	0.0008(4)
Ti	0.020(3)	0.0188(8)	0.003(8)	0.0004(13)
Cr	0.028(3)	0.0151(5)	0.031(8)	0.006(2)
Mn	0.030(3)	0.0146(5)	0.035(8)	0.008(2)
Fe	1.27(2)	0.36(1)	2.1(1)	0.90(3)
Co	0.006(2)	0.00009(4)	0.014(4)	0.009(2)
Ni	0.081(7)	0.0014(3)	0.18(2)	0.19(2)

C2029W,1 (180°)

Element	Raw data (ions/Si ⁺)	Al blank (ions/Si ⁺ _{raw})	Corrected data (ions/Si ⁺)	Corrected data (abd./Si)
Li	0.008(2)	0.00063(5)	0.009(2)	0.0008(2)
Na	29.4(1)	3.931(4)	30.6(1)	1.400(5)
Mg	27.9(1)	0.335(1)	33.2(1)	4.31(2)
Al	180.2(2)	179.66(4)	0.6(3)	0.08(4)
Si	1.00(3)	0.170(3)	1.00(4)	1.00(4)
K	2.33(3)	0.865(2)	1.76(3)	0.048(1)
Ca	2.53(3)	0.0894(6)	2.94(4)	0.215(3)
Sc	0.0025(9)	0.00021(3)	0.003(1)	0.0004(2)
Ti	0.009(4)	0.0103(3)	-0.001(5)	-0.0002(8)
Cr	0.019(3)	0.0169(3)	0.002(3)	0.0004(6)
Mn	0.027(3)	0.0080(2)	0.023(4)	0.0052(8)
Fe	0.66(2)	0.187(6)	0.57(2)	0.24(1)
Co	0.018(3)	0.00008(2)	0.022(3)	0.015(2)
Ni	0.042(4)	0.0020(4)	0.048(5)	0.051(6)

C2086N,1

Element	Raw data (ions/Si ⁺)	Al blank (ions/Si ⁺ _{raw})	Corrected data (ions/Si ⁺)	Corrected data (abd./Si)
Li	0.0005(2)	0.00012(1)	0.0004(2)	0.00003(2)
Na	1.02(1)	0.3255(5)	0.773(8)	0.0353(4)
Mg	8.38(2)	0.0354(2)	9.26(3)	1.202(4)
Al	41.42(5)	40.87(1)	0.61(5)	0.085(8)
Si	1.00(1)	0.098(1)	1.00(2)	1.00(2)
K	0.195(3)	0.0778(3)	0.130(4)	0.0035(1)
Ca	0.113(3)	0.6300(8)	-0.574(3)	-0.0420(3)
Sc	0.0002(1)	0.000078(9)	0.0002(1)	0.00003(2)
Ti	0.0074(8)	0.0017(8)	0.006(1)	0.0011(2)
Cr	0.034(2)	0.00035(2)	0.038(2)	0.0072(3)
Mn	0.0075(7)	0.00203(5)	0.006(1)	0.0014(2)
Fe	0.111(3)	0.043(1)	0.075(3)	0.032(1)
Ni	0.0008(4)	0.00020(9)	0.0007(4)	0.0008(5)

C2086W,1 (0°)

Element	Raw data (ions/Si ⁺)	Al blank (ions/Si ⁺ _{raw})	Corrected data (ions/Si ⁺)	Corrected data (abd./Si)
Li	0.0011(3)	0.00101(4)	0.0001(4)	0.00001(3)
Na	7.22(2)	0.883(1)	9.98(3)	0.456(1)
Mg	2.14(1)	0.2163(7)	3.03(2)	0.393(3)
Al	52.28(5)	51.89(1)	0.61(9)	0.08(1)
Si	1.000(9)	0.365(4)	1.00(2)	1.00(2)
K	0.948(7)	0.564(1)	0.61(1)	0.0164(3)
Ca	0.735(6)	0.3419(8)	0.62(1)	0.0453(8)
Sc	0.0002(1)	0.000040(8)	0.0003(2)	0.00004(3)
Ti	0.024(2)	0.0222(5)	0.004(3)	0.0006(5)
Cr	0.018(1)	0.0144(2)	0.006(2)	0.0011(3)
Mn	0.064(2)	0.0224(2)	0.065(3)	0.0152(7)
Fe	0.640(6)	0.0563(6)	0.92(1)	0.389(4)
Ni	0.009(2)	0.0011(1)	0.013(3)	0.013(3)

C2086W,1 (180°)

Element	Raw data (ions/Si ⁺)	Al blank (ions/Si ⁺ _{raw})	Corrected data (ions/Si ⁺)	Corrected data (abd./Si)
Li	0.0017(5)	0.00038(2)	0.0014(6)	0.00011(5)
Na	26.26(6)	1.042(1)	27.9(1)	1.276(3)
Mg	3.76(3)	0.0922(3)	4.06(3)	0.527(4)
Al	17.07(5)	16.518(4)	0.61(6)	0.085(8)
Si	1.00(1)	0.0967(6)	1.00(1)	1.00(1)
K	0.89(1)	0.2995(6)	0.65(1)	0.0177(4)
Ca	0.64(1)	0.0826(3)	0.61(1)	0.0448(8)
Ti	0.019(2)	0.0051(1)	0.015(2)	0.0026(4)
Cr	0.011(1)	0.00505(8)	0.006(2)	0.0012(3)
Mn	0.032(2)	0.00889(9)	0.025(2)	0.0058(6)
Fe	1.12(1)	0.0243(3)	1.22(2)	0.516(7)
Ni	0.007(3)	0.00027(3)	0.008(3)	0.008(3)

C2091N,1

Element	Raw data (ions/Si ⁺)	Al blank (ions/Si ⁺ _{raw})	Corrected data (ions/Si ⁺)	Corrected data (abd./Si)
Li	0.0014(2)	0.00027(2)	0.0017(4)	0.00014(3)
Na	7.36(2)	0.5324(8)	10.14(3)	0.463(1)
Mg	5.65(2)	0.1008(4)	8.24(3)	1.069(3)
Al	32.78(4)	32.37(1)	0.61(6)	0.085(8)
Si	1.000(7)	0.326(3)	1.00(1)	1.00(1)
K	0.489(5)	0.418(1)	0.104(7)	0.0028(2)
Ca	0.298(4)	0.249(1)	0.073(5)	0.0053(4)
Sc	0.0004(1)	0.000017(6)	0.0006(2)	0.00009(3)
Ti	0.0023(6)	0.0020(3)	0.0004(10)	0.0001(2)
Cr	0.039(1)	0.0178(2)	0.032(2)	0.0061(4)
Mn	0.022(1)	0.0137(1)	0.012(1)	0.0029(3)
Fe	0.45(3)	0.0377(3)	0.61(4)	0.26(2)
Co	0.0003(1)	0.00003(1)	0.0005(2)	0.0003(1)
Ni	0.007(1)	0.00076(6)	0.010(2)	0.010(2)

C2102N,1 #1

Element	Raw data (ions/Si ⁺)	Al blank (ions/Si ⁺ _{raw})	Corrected data (ions/Si ⁺)	Corrected data (abd./Si)
Li	0.0030(2)	0.00051(4)	0.0026(2)	0.00021(1)
Na	11.76(1)	0.405(1)	11.97(1)	0.5469(5)
Mg	10.15(1)	0.0876(5)	10.61(1)	1.377(1)
Al	59.16(2)	58.58(1)	0.61(3)	0.085(4)
Si	1.00(1)	0.0513(8)	1.00(1)	1.00(1)
K	1.878(4)	0.0908(5)	1.884(5)	0.0512(1)
Ca	1.297(3)	0.0571(4)	1.307(4)	0.0957(3)
Ti	0.004(2)	0.0049(1)	0.000(2)	-0.0001(3)
Cr	0.0314(6)	0.00062(4)	0.032(1)	0.0062(1)
Mn	0.0184(6)	0.00090(5)	0.018(1)	0.0043(1)
Fe	0.431(3)	0.036(2)	0.416(4)	0.176(2)
Ni	0.013(1)	0.00011(4)	0.013(1)	0.014(1)

C2102N,1 #2

Element	Raw data (ions/Si ⁺)	Al blank (ions/Si ⁺ _{raw})	Corrected data (ions/Si ⁺)	Corrected data (abd./Si)
Li	0.0016(3)	0.00045(9)	0.0013(4)	0.00011(3)
Na	20.67(4)	0.522(3)	23.51(4)	1.075(2)
Mg	10.35(3)	0.108(1)	11.95(3)	1.552(4)
Al	129.4(1)	128.89(4)	0.6(1)	0.08(2)
Si	1.00(2)	0.143(3)	1.00(2)	1.00(2)
K	1.16(1)	0.093(1)	1.25(1)	0.0339(3)
Ca	2.04(1)	0.120(1)	2.24(1)	0.164(1)
Sc	0.0007(2)	0.00005(3)	0.0008(3)	0.00012(4)
Ti	0.018(3)	0.0100(5)	0.010(3)	0.0016(6)
Cr	0.043(2)	0.0009(1)	0.049(2)	0.0094(4)
Mn	0.029(1)	0.0012(1)	0.032(2)	0.0075(4)
Fe	1.4(1)	0.062(1)	1.6(1)	0.68(3)
Co	0.0023(4)	0	0.0027(5)	0.0018(3)
Ni	0.045(4)	0.0004(2)	0.052(4)	0.055(5)

C2102N,1 #2.1

Element	Raw data (ions/Si ⁺)	Al blank (ions/Si ⁺ _{raw})	Corrected data (ions/Si ⁺)	Corrected data (abd./Si)
Li	0.0014(7)	0.0009(2)	0.001(1)	0.00005(8)
Na	46.2(1)	1.006(5)	62.4(2)	2.850(8)
Mg	14.8(1)	0.209(3)	20.2(1)	2.62(1)
Al	248.8(3)	248.4(1)	0.6(4)	0.08(6)
Si	1.00(3)	0.276(6)	1.00(4)	1.00(4)
K	1.80(2)	0.179(2)	2.24(3)	0.061(1)
Ca	3.43(3)	0.231(3)	4.41(5)	0.323(3)
Sc	0.0006(4)	0.00009(6)	0.0007(6)	0.0001(1)
Ti	0.024(6)	0.0194(9)	0.007(8)	0.001(1)
Cr	0.039(4)	0.0018(3)	0.052(5)	0.010(1)
Mn	0.031(3)	0.0022(3)	0.040(4)	0.009(1)
Fe	3.4(2)	0.120(2)	4.5(2)	1.9(1)
Co	0.0012(6)	0	0.002(1)	0.0011(6)
Ni	0.017(5)	0.0009(3)	0.022(6)	0.023(7)

C2102N,1 #2.2

Element	Raw data (ions/Si ⁺)	Al blank (ions/Si ⁺ _{raw})	Corrected data (ions/Si ⁺)	Corrected data (abd./Si)
Li	0.017(7)	0.0006(1)	0.0014(9)	0.00011(7)
Na	15.93(6)	0.700(4)	18.86(8)	0.862(4)
Mg	8.72(5)	0.145(2)	10.61(7)	1.38(1)
Al	173.4(2)	172.9(1)	0.6(3)	0.08(4)
Si	1.00(2)	0.192(4)	1.00(3)	1.00(3)
K	1.25(2)	0.124(2)	1.39(2)	0.038(1)
Ca	1.57(2)	0.161(2)	1.74(3)	0.127(2)
Sc	0.0005(4)	0.00006(4)	0.0005(5)	0.00009(7)
Ti	0.016(2)	0.0135(7)	0.004(3)	0.0006(5)
Cr	0.027(3)	0.0012(2)	0.032(4)	0.006(1)
Mn	0.026(3)	0.0016(2)	0.031(3)	0.007(1)
Fe	1.10(8)	0.084(2)	1.3(1)	0.53(4)
Co	0.005(1)	0	0.006(1)	0.004(1)
Ni	0.089(6)	0.0006(2)	0.109(7)	0.12(1)

C2102N,1 #2.3

Element	Raw data (ions/Si ⁺)	Al blank (ions/Si ⁺ _{raw})	Corrected data (ions/Si ⁺)	Corrected data (abd./Si)
Li	0.0018(4)	0.00026(5)	0.0017(4)	0.00014(3)
Na	12.35(3)	0.310(2)	13.16(3)	0.602(2)
Mg	8.06(3)	0.064(1)	8.74(3)	1.135(4)
Al	77.05(8)	76.49(3)	0.61(9)	0.08(1)
Si	1.00(1)	0.085(2)	1.00(1)	1.00(1)
K	0.793(8)	0.055(1)	0.81(1)	0.0219(2)
Ca	1.45(1)	0.071(1)	1.51(1)	0.111(1)
Sc	0.0005(2)	0.00003(2)	0.0006(2)	0.00009(4)
Ti	0.013(2)	0.0060(3)	0.008(2)	0.0013(4)
Cr	0.042(2)	0.00055(8)	0.045(2)	0.0087(4)
Mn	0.024(1)	0.00069(8)	0.025(2)	0.0058(4)
Fe	0.70(3)	0.0370(7)	0.73(4)	0.31(3)
Co	0.0011(3)	0	0.0012(3)	0.0008(2)
Ni	0.033(3)	0.0003(1)	0.036(3)	0.038(3)